Interaction of microphysics and dynamics in a warm conveyor belt simulated with the ICON model

Annika Oertel[1], Annette K Miltenberger[2], Christian M Grams[1], and Corinna Hoose[1]

[1]Institute of Meteorology and Climate Research, Karlsruhe Institute of Technology
[2]Institute for Atmospheric Physics, Johannes Gutenberg University Mainz

Correspondence: Annika Oertel (annika.oertel@kit.edu)

Abstract. Warm conveyor belts (WCBs) produce the major fraction of precipitation in extratropical cyclones and modulate the large-scale extratropical circulation. Diabatic processes, in particular associated with cloud formation, influence the cross-isentropic ascent of WCBs into the upper troposphere and additionally modify the potential vorticity (PV) distribution, which influences the larger-scale flow. In this study we investigate diabatic heating and PV rates from all physics processes, including microphysics, turbulence, convection, and radiation, in a case study that occurred during the North Atlantic Waveguide and Downstream Impact Experiment (NAWDEX) campaign using the Icosahedral Nonhydrostatic (ICON) modelling framework. In particular, we consider all individual microphysical process rates that are implemented in ICON's two-moment microphysics scheme, which sheds light on (i) which microphysical processes dominate the diabatic heating and PV structure in the WCB, and (ii) which microphysical processes are most active during the ascent and influence cloud formation and characteristics, providing a basis for detailed sensitivity experiments. For this purpose, diabatic heating and PV rates are integrated for the first time along online trajectories across nested grids with different horizontal resolutions. The convection-permitting simulation setup also takes the reduced aerosol concentrations over the North Atlantic into account. Our results confirm that microphysical processes are the dominant diabatic heating source during ascent. Near cloud top longwave radiation cools WCB air parcels. Radiative heating, and corresponding PV modification in the upper troposphere, are non-negligible due to the longevity of the WCB cloud band. In the WCB ascent region, the process rates from turbulence and microphysics partially counteract each other. From all microphysical processes condensational growth of cloud droplets and vapor deposition on frozen hydrometeors most strongly influence diabatic heating and PV, while below-cloud evaporation strongly cools WCB air parcels prior to their ascent and increases their PV value. PV production is strongest near the surface with substantial contributions from condensation, melting, evaporation, and vapor deposition. In the upper troposphere, PV is reduced by diabatic heating from vapor deposition, condensation, and radiation. Activation of cloud droplets as well as homogeneous and heterogeneous freezing processes have a negligible diabatic heating contribution, but their detailed representation is important for, e.g., hydrometeor size distributions. Generally, faster ascending WCB trajectories are heated markedly more than more slowly ascending WCB trajectories, which is linked to larger initial specific humidity content providing a thermodynamic constraint on total microphysical heating. Yet, the total diabatic heating contribution of convectively ascending trajectories is relatively small due to their small fraction in this case study. Our detailed case study documents the effect of different microphysical processes implemented in ICON's two-moment scheme for heating and PV rates in a WCB from a joint Eulerian and Lagrangian perspective. It emphasizes

the predominant role of microphysical processes and provides a framework for future experiments on cloud-microphysical sensitivities in WCBs.

1 Introduction

Extratropical cyclones (ETCs) are often characterized by a vertically-extended cloud band in their warm sector with a long-lived cirrus shield, which is formed by a strongly ascending airstream, the so-called warm conveyor belt (WCB, Wernli and Davies, 1997; Eckhardt et al., 2004; Madonna et al., 2014; Oertel et al., 2019). WCBs are responsible for the major part of precipitation associated with ETCs (Pfahl et al., 2014), interact with and modify the upper-level flow (Grams et al., 2011; Rodwell et al., 2017; Grams et al., 2018; Berman and Torn, 2019; Oertel et al., 2023), and influence the extratropical cloud radiative forcing (Joos, 2019). During the WCB's ascent from the lower into the upper troposphere a wide range of cloud processes take place, ranging from warm-phase to mixed-phase and ice-phase processes (Forbes and Clark, 2003; Joos and Wernli, 2012; Crezee et al., 2017; Gehring et al., 2020; Mazoyer et al., 2021, 2023). The representation of cloud processes is one of the key challenges in numerical weather prediction ((NWP); e.g., Khain et al., 2015; Dearden et al., 2016; Hande and Hoose, 2017; Field et al., 2017) and influences cloud characteristics, dynamics and surface precipitation. Hence, uncertainty in microphysical processes may modify a WCB's cloud and precipitation structure. For example, cloud condensation nuclei (CCN) concentrations affect cloud internal dynamics and surface precipitation in convective systems (e.g. Seifert and Beheng, 2006b; Noppel et al., 2010; Barthlott and Hoose, 2018; Igel and van den Heever, 2021; Barthlott et al., 2022). The response to changing CCN concentrations is not unidirectional and depends on the applied NWP model and microphysics scheme, as well as on the synoptic conditions (Tao et al., 2012; Fan et al., 2016). Due to the very different dynamics and associated microphysical process pathways between convective systems and large-scale WCB ascent in extratropical cyclones, these results cannot directly be transferred to WCBs where updraft velocities are substantially smaller and markedly influenced by synoptic conditions. A climatological comparison of precipitation characteristics during WCB ascent in polluted versus clean conditions in a simulation with a relatively low spatial resolution of $1.875° \times 1.875°$ showed only a small impact of aerosols on WCB associated surface precipitation (Joos et al., 2017), whereby polluted conditions slightly delayed precipitation formation. Observations and idealized numerical model simulations suggest that the cloud liquid water path in WCBs is influenced to some extent by the cloud droplet number concentration (CDNC), which modifies cloud albedo (McCoy et al., 2018), and thus the cloud radiative forcing. In the upper troposphere the microphysical and macrophysical properties of cirrus clouds also substantially affect cloud radiative forcing (e.g., Zhang et al., 1999; Joos et al., 2014), which to some extent depends on the formation pathways of the cirrus clouds (Krämer et al., 2016; Luebke et al., 2016; Wernli et al., 2016).

Aside from modifying cloud properties, microphysical processes and their associated latent heating play an important role in the dynamics and structure of extratropical cyclones (e.g., Reed et al., 1992; Rossa et al., 2000; Wernli et al., 2002; Binder et al., 2016). Uncertainty in the representation of latent heat release can represent a dominant source of initial error growth (Baumgart et al., 2019). In general, WCBs influence the large-scale flow through both direct PV modification in the lower and upper troposphere (e.g., Rossa et al., 2000; Pomroy and Thorpe, 2000; Joos and Forbes, 2016; Oertel et al., 2020; Mazoyer

et al., 2021) and their related divergent outflow in the upper troposphere (e.g., Grams and Archambault, 2016; Steinfeld and Pfahl, 2019; Teubler and Riemer, 2021).

The latter is strongly linked to the WCB ascent strength and its isentropic outflow level, which again is driven by latent heat release. Thus uncertainty in the representation of latent heat release substantially influences the WCB's cross-isentropic ascent and the WCB's impact on the large-scale upper-level flow (e.g., Martínez-Alvarado et al., 2014; Schäfler and Harnisch, 2015; Joos and Forbes, 2016; Mazoyer et al., 2021; Pickl et al., 2022) which might lead to forecast busts (Grams et al., 2018).

Moreover, WCB-related diabatic heating modifies the PV distribution in extratropical cyclones (see, e.g., Wernli and Davies, 1997; Joos and Wernli, 2012; Spreitzer et al., 2019; Attinger et al., 2019; Rivière et al., 2021, for more details). On larger scales, where vertical diabatic heating gradients dominate, diabatic heating during slantwise WCB ascent increases low-level PV values, which can lead to an intensification of cyclones (Rossa et al., 2000; Joos and Wernli, 2012; Binder et al., 2016). In the upper troposphere, PV values are decreased, which can modify the upper-level flow evolution (e.g., Wernli and Davies, 1997; Pomroy and Thorpe, 2000; Grams et al., 2011; Madonna et al., 2014; Methven, 2015; Saffin et al., 2021). Hence, as ascending air parcels pass through the quasi-vertical PV dipole related to mid-tropospheric diabatic heating from cloud formation, their PV values on average increase before they decrease to values close to their initial PV value (e.g., Madonna et al., 2014; Methven, 2015). On smaller scales, horizontal diabatic heating gradients become increasingly important and form quasi-horizontal PV dipoles in an environment where vertical wind shear is aligned with smaller-scale horizontal diabatic heating gradients (Chagnon and Gray, 2009; Harvey et al., 2020; Oertel et al., 2020, 2021). These smaller-scale PV anomalies are particularly relevant for convective activity embedded in the WCB airstream and can modify the meso-scale circulation (Oertel et al., 2020, 2021; Oertel and Schemm, 2021). Case studies showed that the major contribution to the PV modification from microphysics results from condensation and vapor deposition on frozen hydrometeors in the lower and upper troposphere, respectively (Joos and Wernli, 2012; Joos and Forbes, 2016; Mazoyer et al., 2021, 2023), and point towards sensitivities on the model representation of ice-phase (Mazoyer et al., 2021) and mixed-phase microphysics (Mazoyer et al., 2023).

In summary, uncertainty related to the parameterisation of microphysical processes influences the WCB cloud structure as well as the associated diabatic heating and PV structure, both important factors for NWP. Previous case studies applying one-moment or quasi two-moment microphysics schemes showed that the detailed WCB ascent and net diabatic heating vary depending on the applied microphysics scheme, the NWP model, and the WCB case (Martínez-Alvarado et al., 2014; Joos and Forbes, 2016; Mazoyer et al., 2021; Choudhary and Voigt, 2022; Mazoyer et al., 2023). An improved understanding of individual processes relevant for the cloud structure and diabatic heating in a WCB and in different models, will facilitate the identification of microphysical processes and related model parameters that are uncertain but particularly relevant for WCB ascent. For example, detailed sensitivity studies typically rely on the selection of a few uncertain parameters. Understanding which processes are active, interact, and influence diabatic heating and the cloud structure provides added value for targeted parameter selection.

Building upon aforementioned studies focusing on one-moment and/or quasi-two moment schemes, this study aims to yield a consistent and detailed view on microphysical processes, their interactions, and partially compensating processes in a two-moment microphysics scheme in the ICON model (Zängl et al., 2015), which may - aside from enhanced physical understand-

95 ing - ultimately contribute to model development and ensemble configuration (e.g., Ollinaho et al., 2017). Specifically, we combine Lagrangian and Eulerian perspectives to quantify diabatic heating and PV rates considering diabatic heating contributions from all physics parameterisations with a strong focus on individual microphysical process rates represented in ICON's two-moment scheme (Seifert and Beheng, 2006a). We address the following research questions:

1. Which non-conservative processes dominate the total diabatic heating in a WCB case study?

100 2. Which microphysical processes are active during WCB ascent in the two-moment scheme, and how large are their individual contributions to the total diabatic heating?

3. What is the influence of the non-conservative processes on the PV distribution in the WCB?

The study is structured as follows: We first introduce the ICON model and novel Lagrangian and Eulerian diagnostics (Section 2). Section 2 also explains the modifications to the CCN activation scheme to account for reduced aerosol concentrations in the North Atlantic region. Next, we introduce the WCB case study (Section 3) and quantify the total integrated diabatic heating associated with the individual (micro-)physics processes (Section 4). Before concluding with a summary (Section 6), we show the processes that impact the spatio-temporal PV structure of the WCB using complementary Lagrangian and Eulerian perspectives (Section 5).

2 Methods

110 Diabatic processes in a WCB case study and their impact on the PV structure are investigated in a high-resolution ICON simulation. Lagrangian metrics providing insight into WCB air parcel history are combined with an Eulerian perspective providing spatial context for the WCB air parcel analysis. The following describes the numerical model including the individual microphysical processes from the two-moment scheme (Sections 2.1-2.2) and model diagnostics used in our analysis, i.e. diabatic heating and PV rates (Section 2.4) and online trajectories (Section 2.5) applied for the first time including trajectory transfer across refined grids. Details on the composite analysis of WCB related cloud characteristics used for the Eulerian analysis are provided in Section 2.6. To account for aerosol concentrations over the North Atlantic we modify the CCN activation scheme, which is briefly described in Section 2.3 and in more detail in Section A.

2.1 ICON model setup

We employ the Icosahedral Nonhydrostatic (ICON) modelling framework (version 2.6.2.2; Zängl et al., 2015) to simulate a
120 WCB case that occurred in the North Atlantic in October 2016 during the NAWDEX campaign (IOP 7; Schäfler et al., 2018). The WCB case was selected as it is associated with a large-scale and strongly amplified downstream ridge (Section 3) and also due to the availability of airborne observations of aerosol concentrations (Appendix A). We run a global simulation with a R03B07 grid (approx. 13 km effective grid spacing, corresponding to the operational resolution of the global ICON model setup used by the German weather service) and with a time step of 120 s. Additionally, two higher resolution refined domains are

nested in the global simulation on R03B08 and R03B09 grids (approx. 6.5 km and 3.3 km effective grid spacing, Fig. 1). The time step for the refined nests is by definition halved from the respective lower resolution parent domain, i.e., 60 s and 30 s. The higher resolution simulations are coupled by two-way nesting to the next lower resolution simulation, i.e., the lower resolution simulation provides lateral boundary conditions for the next higher resolution nest at every time step, and in turn, the lower resolution prognostic fields are nudged towards the solution from the respective higher resolution. The first refined domain encompasses the major part of WCB inflow, ascent and outflow region (R03B08 grid with approx. 6.5 km), and the second higher-resolution domain (R03B09 grid with approx. 3.3 km) is nested in the first one and focuses on the WCB ascent region (Fig. 1). The vertical dimension is represented by terrain-following smooth level vertical (SLEVE) coordinates (Leuenberger et al., 2010) with 90 levels. Level number is identical in all nests, but the coordinate systems in higher-resolution nests reflect the higher resolution of topography. The simulation is initialized from the ECMWF analysis at 18 UTC 03 October 2016 and runs freely for 72 h. Deep convection is treated explicitly in the nested domains, and the Tiedtke-Bechtold convection scheme is used for the global domain (Tiedtke, 1989; Bechtold et al., 2008; ECMWF, 2016). Shallow convection is parameterised in all domains. Turbulence (Raschendorfer, 2018) and sub-grid scale orographic drag (Lott and Miller, 1997) and non-orographic gravity wave drag (Orr et al., 2010) are parameterised by the standard schemes used in ICON. Radiation is described by the Rapid Radiative Transfer Model (RRTM; Mlawer et al., 1997). Cloud microphysical processes are represented by a two-moment microphysics scheme (Seifert and Beheng, 2006a) with six hydrometeor types (cloud, ice, rain, snow, graupel, and hail) and prognostic variables for the hydrometeor mass mixing ratios (cloud liquid (q_c), ice (q_i), rain (q_r), snow (q_s), graupel (q_g), and hail (q_h)), and corresponding number concentrations.

2.2 Microphysical processes

We focus on the microphysical processes that are associated with phase changes of water, and hence diabatic heating or cooling (and do not explicitly analyse adiabatic processes such as accretion, autoconversion, or ice collision processes). In the following, the microphysical processes are discussed in the order in which they are called in ICON, complemented by temperature tendencies from the other physics parameterisations in ICON.

– Saturation adjustment I (SATAD I)

The saturation adjustment removes sub- or super-saturation with respect to liquid water and establishes thermodynamic equilibrium between water vapor and liquid water by condensation or evaporation of cloud droplets, respectively, assuming that clouds relax instantly to a thermodynamic equilibrium. In ICON the saturation adjustment is called twice: Once before the explicit microphysical processes, and once afterwards.

– Turbulence scheme (TURB)

Turbulent diffusion in the free troposphere is represented by a 2nd order closure scheme developed by Raschendorfer (2018) which uses a prognostic equation for turbulent kinetic energy.

- CCN activation (QCACT)

  The activation of CCN is based on a modification of the Hande et al. (2016) parameterisation (see Section 2.3 and Appendix A for details).

- Homogeneous and heterogeneous ice nucleation (QIFRZ)

  Homogeneous freezing is parameterised following Kärcher and Lohmann (2002) and Kärcher et al. (2006). The heterogeneous freezing parameterisation is adapted from Hande et al. (2015) and includes parameterisations for immersion and deposition freezing. Their freezing rates increase with decreasing temperature. If cloud droplets are present, immersion freezing is active below -12°C. Deposition nucleation takes place in a temperature range from -20°C to -53°C and is scaled by grid-scale variables, such as supersaturation w.r.t. ice.

- Homogeneous freezing of cloud droplets (QCFRZ)

  Freezing of cloud droplets is described by a homogeneous freezing rate increasing exponentially with decreasing temperature (Jeffery and Austin, 1997). Below -50°C all cloud droplets freeze immediately.

- Depositional growth of all ice-phase hydrometeors (QXDEP)

  Deposition of vapor on and sublimation from frozen hydrometeors is computed with a relaxation time-scale approach (Morrison et al., 2005). The deposition parameters are calculated for the four ice hydrometeor types (ice, snow, graupel, and hail) explicitly. We individually consider diabatic heating from vapor deposition on ice (QIDEP), snow (QSDEP), and the sum of vapor deposition on graupel and hail (QGDEP).

- Riming (QXRIM)

  Riming is treated explicitly between the individual hydrometeor types (see Seifert and Beheng, 2006a). A fraction of the rimed mass is redistributed to smaller ice particles if the temperature conditions for the Hallet and Mossop ice multiplication process are met, but this is not associated with any additional latent heat release. We consider heating from the sum of all individual riming processes.

- Freezing of rain (QRFRZ)

  The hetereogeneous freezing rate of rain increases with decreasing temperature and increasing mean rain drop mass following Bigg (1953). Below -40°C all rain instantly freezes.

- Melting of ice hydrometeors (QXMLT)

  Above 0°C frozen hydrometeors melt. Melting rates for snow, graupel and hail are represented explicitly, while all cloud ice melts immediately. Above 10°C all snow immediately melts, too. We consider the sum of all melting processes.

- Evaporation of melting ice hydrometeors (QSGHEVAP)

  Above 0°C, liquid surfaces of melting ice hydrometeors can evaporate (Seifert and Beheng, 2006a). Evaporation of melting ice hydrometeors is treated similar to evaporation of rain with a constant surface temperature of 273 K. Again we consider the sum of the processes rates for snow, graupel, and hail.

- Evaporation of rain (QREVAP)

    Evaporation of rain in subsaturated conditions is based on a parameterisation by Seifert (2008) taking into account the rain drop size distribution which, e.g., allows smaller rain drops to evaporate faster.

- Second saturation adjustment (SATAD II)

    The second saturation adjustment after the explicit microphysical processes is called to start the subsequent slow-physics parameterisations in an equilibrated state.

- Slow physics parameterisations

    The slow physics processes are only called at a reduced frequency, and include parameterisations of convection (CON, dt=600 s), radiation (RAD, dt=1800 s, and non-orographic and orographic gravity wave drag (DRAG, dt=600 s). Furthermore, radiation is calculated from a coarser grid (R03B06). Diabatic temperature tendencies from these processes are also considered in our analysis.

2.3 CCN activation

The recently developed CCN activation scheme (Hande et al., 2016) for the ICON model is optimized for aerosol number concentrations over Germany and based on extensive campaign measurements of aerosol size distributions over land. However, air mass characteristics over continental regions can differ substantially from those over the open ocean (Hudson and Xie, 1999; Wang et al., 2021). As the representation of aerosol concentrations and associated CCN activation influences the cloud droplet number concentration, this can influence WCB cloud characteristics (McCoy et al., 2018). To account for the substantially differing aerosol characteristics over the North Atlantic compared to continental Germany, we modified the CCN activation parameterisation based on airborne measurements of size-resolved aerosol number concentrations from three research flights of the British Facility for Airborne Atmospheric Measurements (FAAM) BAe 146 that took place during the NAWDEX campaign in September and October 2016 (CEDA, Facility for Airborne Atmospheric Measurements; Natural Environment Research Council; Met Office, 2016a, b, c; CEDA, Centre for Environmental Data Analysis, 2016). Based on the observed aerosol size distributions a modified parameterisation of CCN activation was developed that provides the number of activated cloud droplets N_c as a function of vertical velocity w and pressure p (see Appendix A for details):

$$N_c(w,p) = N_a(p) \cdot \left(1 + e^{-B(p) \cdot ln(w) - C(p)}\right)^{-1} \qquad (1)$$

where $N_a(p)$ is the number concentration of aerosols estimated from the observational data and $B(p)$, $C(p)$ are determined by detailed parcel model simulations of CCN activation (including explicit representation of super-saturation evolution). CCN activation was limited to temperatures above -38 °C to prevent production of very large ice number concentrations by CCN activation at low temperatures and immediate subsequent homogeneous freezing of the activated cloud droplets.

Vertical profiles of the predicted CCN number densities from the original parameterisation by Hande et al. (2016) (dashed lines) and our modified version (solid lines) are shown in Fig. 2. Both parameterisations have a distinct dependence of CCN
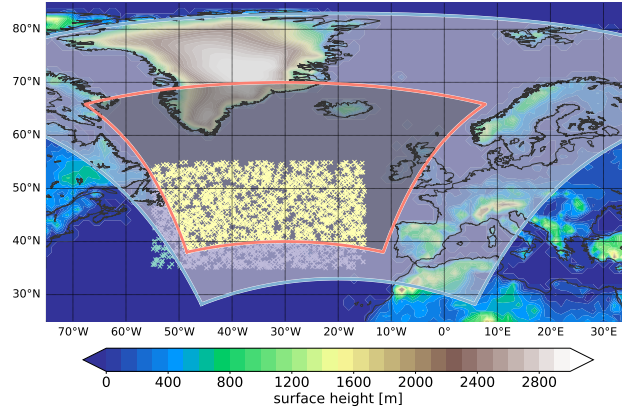
Figure 1. Refined nested domains and trajectory starting position in the global domain (R03B07, green 'x'), in the first refined nest (R03B08, purple 'x'), and in the second refined convection-permitting nest (R03B09, yellow 'x'). Domain boundaries of both refined nests are shown in blue and red and yellow. The shading shows the surface altitude (in m).

number density on vertical velocity (colors) and pressure. The new parameterisation reflects broadly lower CCN concentrations over the North Atlantic compared to Central Europe. However, aerosol concentrations over the North Atlantic are subject to substantial variability (as already evident from the three flights shown in Fig. A1c and used here). This variability cannot be captured by the parameterisation, but for future analysis, systematic sensitivity experiments with varying CCN concentrations taking into account the variability of aerosol number concentrations will be performed.

Appendix B provides a comparison of two limited-area simulations applying the modified and original CCN activation schemes. While qualitatively the key diabatic heating contributions do not significantly depend on the adjustment of the CCN activation scheme, this provides a baseline for subsequent detailed CCN sensitivity experiments with more realistic assumptions about marine CCN variability.

2.4 Diabatic heating and PV rates

Latent heat release during phase changes of water is associated with diabatic heating. We calculate potential temperature tendencies from all individual microphysical processes described in Section 2.1 following Joos and Wernli (2012). The diabatic heating rates (DHR) are defined for each individual microphysical process as

$$DHR = \frac{D\theta}{Dt} = S_j * \frac{l_j}{c_p} \cdot \left(\frac{p_0}{p}\right)^{\kappa} \tag{2}$$

with the individual microphysical process rates S_j (i.e., the hydrometeor source and sink terms of the respective microphysical processes listed in Table 1 and Section 2.1), and the according latent heat of freezing ($l_f = 3.337 \cdot 1e5\,\mathrm{J\,kg^{-1}}$), sublimation ($l_s = 2.8345 \cdot 1e6\,\mathrm{J\,kg^{-1}}$) or vaporization ($l_v = 2.5008 \cdot 1e6\,\mathrm{J\,kg^{-1}}$), the specific heat at constant pressure $c_p = 1004.64\,\mathrm{J\,kg^{-1}\,K^{-1}}$, the potential temperature θ, and $\kappa = \frac{R}{c_p}$, with the specific gas constant of air R=287 $\mathrm{J\,kg^{-1}\,K^{-1}}$.
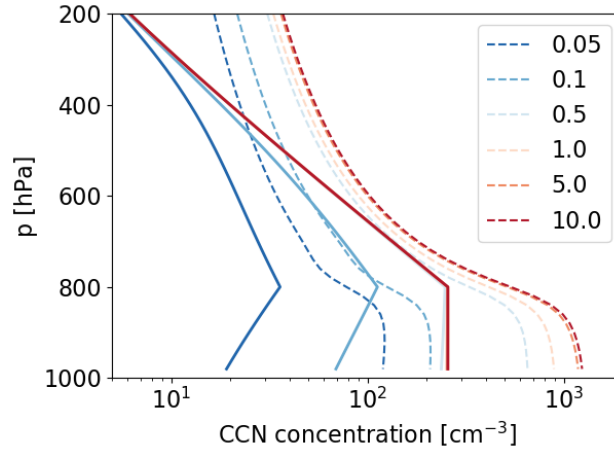
Figure 2. Vertical profiles of original (dashed) and modified (solid) parameterised CCN concentration (in cm^{-3}) for different vertical velocities (colours, in m s^{-1}).

Analogously, the instantaneous PV rates (PVR) from individual microphysical processes are calculated (e.g., Joos and Wernli, 2012; Crezee et al., 2017; Spreitzer et al., 2019) as

$$PVR = \frac{DPV}{Dt} = \frac{1}{\rho} \cdot \left(\zeta \cdot \nabla \frac{D\theta}{Dt} \right), \tag{3}$$

240 with

$$PV = \frac{1}{\rho} \cdot (\zeta \cdot \nabla \theta), \tag{4}$$

where ρ is density, and ζ is the 3D vorticity vector.

For comparison, bulk diabatic heating and related PV tendencies from other parameterisation schemes, i.e. long- and short-wave radiation, turbulence, convection, and drag, are also considered (Table 1). Note that eq. 3 neglects the change of PV from 245 momentum tendencies ($\frac{\partial u}{\partial t}, \frac{\partial v}{\partial t}, \frac{\partial w}{\partial t}$), which can arise from friction, diffusion, and turbulence (Spreitzer et al., 2019; Rivière et al., 2021). Thus, the modification of PV through momentum tendencies that are parameterised in the turbulence, convection and drag schemes are not included in this analysis.

2.5 Online trajectories

Although WCBs are large-scale airstreams that can readily be identified with offline trajectories, i.e. trajectories calculated 250 after the model simulation based on low time resolution wind field output, recent studies employed high-resolution online trajectories to represent smaller-scale heterogeneities in the WCB cloud band (e.g., Rasp et al., 2016; Oertel et al., 2020, 2021; Blanchard et al., 2020). These trajectories are computed during the model simulation, i.e. solving the trajectory equation with the actual wind fields at each model timestep. A high temporal resolution of the solution is particularly useful if detailed mi-

crophysical processes are considered (Miltenberger et al., 2016, 2020; Mazoyer et al., 2021). The major advantages of using online trajectories for this study are (i) the wind fields which are used to compute the trajectory position are considered at every model time step, and (ii) the microphysical process rates are integrated online at every model time step (eq. 5). The available online trajectory module in ICON (Miltenberger et al., 2020) is based on the COSMO online trajectory module (Miltenberger et al., 2013, 2014) with modifications to accommodate the unstructured ICON grid.

In the two-way nested simulations we use here, it is not sufficient to follow air parcels in only one nest, if the full evolution of the WCB from pre-ascent to outflow is of interest which covers a scale of approximately 1000 km. Therefore, we implemented nesting support in the ICON online trajectory module, i.e. for the first time trajectories are allowed to enter or leave a refined nest, and are passed on across the border of the nest. The trajectories' positions and properties are always calculated from the resolved wind fields in the nest with the highest spatial resolution at a given geolocation and using the corresponding model time step. This way, trajectories profit from the high-resolution in the refined nest, however, are not limited to this region. As the trajectory positions are calculated from resolved wind fields, convective updrafts parameterised by the deep convection scheme used in the global domain cannot be explicitly represented.

To reduce the number of trajectories, starting positions are limited to six vertical levels between 200 and 1500 m, and approximately 1900 longitude and latitude positions pre-defined based on offline WCB calculations with LAGRANTO (Sprenger and Wernli, 2015) for this case study (Fig. 1). The starting region between -55°E to -15°N and 35°N to 55°N encompasses all three domains, however, the largest number of trajectories start in the inner-most convection-permitting nest which covers the main WCB ascent region. In total, approximately 11 500 online trajectories are started every 1 h during the 72 h simulation.

Along online trajectories we compute the accumulated diabatic heating ADH and PV change APV, similar to the methodology developed and applied by Crezee et al. (2017); Spreitzer et al. (2019); Attinger et al. (2019) for offline trajectories. Accumulated heating and PV change is defined by the sum of instantaneous rates along the path of the trajectory at every domain-specific model time step Δt, i.e., 120 s, 60 s, and 30 s for the global domain and both refined nests, respectively (see Section 2.1).

$$ADH(\mathbf{x}(t),t) = \sum_{i=1}^{n} DHR(\mathbf{x}(t_i),t_i)\Delta t, \tag{5}$$

$$APV(\mathbf{x}(t),t) = \sum_{i=1}^{n} PVR(\mathbf{x}(t_i),t_i)\Delta t, \tag{6}$$

with $i = 1$ corresponding to initialization of each trajectory and $n = t_{end} - t_{init}$ being the length of the trajectory (difference between initialization time t_{init} of each trajectory and end time of the ICON simulation t_{end}). Trajectory position and properties (Table 1) are subsequently output every 15 minutes.

Table 1. List of available variables along online trajectories. The variables are grouped in (i) atmospheric state variables (whose values are output instantaneously), (ii) integrated diabatic heating rates (ADH), and (iii) integrated diabatic PV rates (APV).

abbreviation	variable
lon, lat, alt	longitude, latitude, altitude
p, ρ, t, q_v	pressure, air density, temperature, specific humidity
q_c, q_r, q_i, q_s, q_g	cloud, rain, ice, snow, graupel water content
PV	potential vorticity
ADH_{SATADI}, $ADH_{SATADII}$	ADH from first and second saturation adjustment
ADH_{QSDEP}, ADH_{QIDEP}, ADH_{QXDEP}	ADH from vapor deposition on snow, ice and sum of all frozen hydrometeors
ADH_{QXRIM}	ADH from all riming processes
ADH_{QCACT}	ADH from CCN activation
ADH_{QREVAP}, $ADH_{QSGHEVAP}$	ADH from evaporation of rain and of melting ice hydrometeors
ADH_{QRMLT}, ADH_{QCMLT}, ADH_{QXMLT}	ADH from melting of frozen hydrometeors into rain and cloud droplets, and the respective sum
ADH_{QRFRZ}	ADH from freezing of rain
ADH_{QCFRZ}	ADH from homogeneous freezing of cloud droplets
ADH_{QIFRZ}	ADH from homogeneous and heterogeneous ice nucleation
ADH_{LW}, ADH_{SW}	ADH from long- and shortwave radiation
ADH_{CON}, ADH_{TURB}, ADH_{DRAG}	ADH from convection, turbulence, and drag parameterisation
APV_{SATADI}, $APV_{SATADII}$	APV from first and second saturation adjustment
APV_{QXDEP}	APV from vapor deposition on ice, snow, graupel and hail
APV_{QXRIM}	APV from all riming processes
APV_{QCACT}	APV from CCN activation
APV_{QREVAP}	APV from evaporation of rain
APV_{QRMLT}	APV from melting of frozen hydrometeors into rain
APV_{RAD}, APV_{CON}, APV_{TURB}	APV from long- plus shortwave radiation, convection and turbulence parameterisation

From all online trajectories, we select WCB trajectories as trajectories with an ascent rate of at least 600 hPa in 48 h (Wernli and Davies, 1997; Madonna et al., 2014; Oertel et al., 2019), and subsequently define the ascent phase as the period encompassing the fastest 600 hPa ascent. This 600 hPa ascent phase can be described by a timescale (τ_{600}), which defines the minimum time required to ascend 600 hPa (Oertel et al., 2021).

The start of the fastest 600 hPa ascent (t_0) along each trajectory is defined as the start of WCB ascent. To compare the heating among trajectories with differing length prior to t_0, ADH is set to 0 at the start of the fastest 600 hPa ascent phase, i.e., ADH at t_0 is subtracted from ADH.

2.6 Front-relative WCB composites

In addition to the trajectory perspective, we consider cold front-relative vertical cross-section composites across the WCB cloud band, which encompasses a primary WCB ascent region (see Section 3 for details). Figure 3a-c (black markers) illustrates WCB air parcel locations ascending in the cyclones warm sector ahead of the front, and Figure 3d-f shows the corresponding large-scale cloud band. Therefore, West-East oriented vertical cross-section composites are considered, which are centred at the western edge of the WCB ascent region identified from Eulerian model fields by the convolutional neural network (CNN) model for WCB ascent 'ELIAS 2.0' (Quinting and Grams, 2022). The CNN model computes conditional WCB ascent probabilities based on the distribution of horizontal wind speed, temperature, geopotential, and specific humidity on selected pressure levels which are taken from the global ICON simulation and were interpolated to a regular $1.0° \times 1.0°$ grid. As shown by Quinting and Grams (2022), 'ELIAS 2.0' adequately represents the WCB ascent footprint and provides a smooth mask of the WCB ascent region. Quinting et al. (2022) compared WCB ascent footprints based on coarse-grained Eulerian fields from a high-resolution ICON simulation with offline trajectories that were computed from a $0.1° \times 0.1°$ grid and found a good agreement between the location of trajectory ascent and the CNN-based footprint. Section 3 and Fig. 3 illustrate that this also applies to the online trajectories.

The vertical cross-section composites are calculated from individual zonal cross-sections through the WCB ascent region ahead of the cold front (here defined as region where the conditional probability of the CNN exceeds 0.3; Quinting and Grams, 2022) using data from the first refined nest (R03B08) with a zonal grid spacing of $0.1°$. The composites include all individual cross-sections within the latitudinal band covered by the CNN ascent mask during 04 to 05 Oct. The cross-section composites illustrate the vertical cloud structure associated with the ascending WCB airstream, and demonstrate the spatial distribution of diabatic heating and PV change.
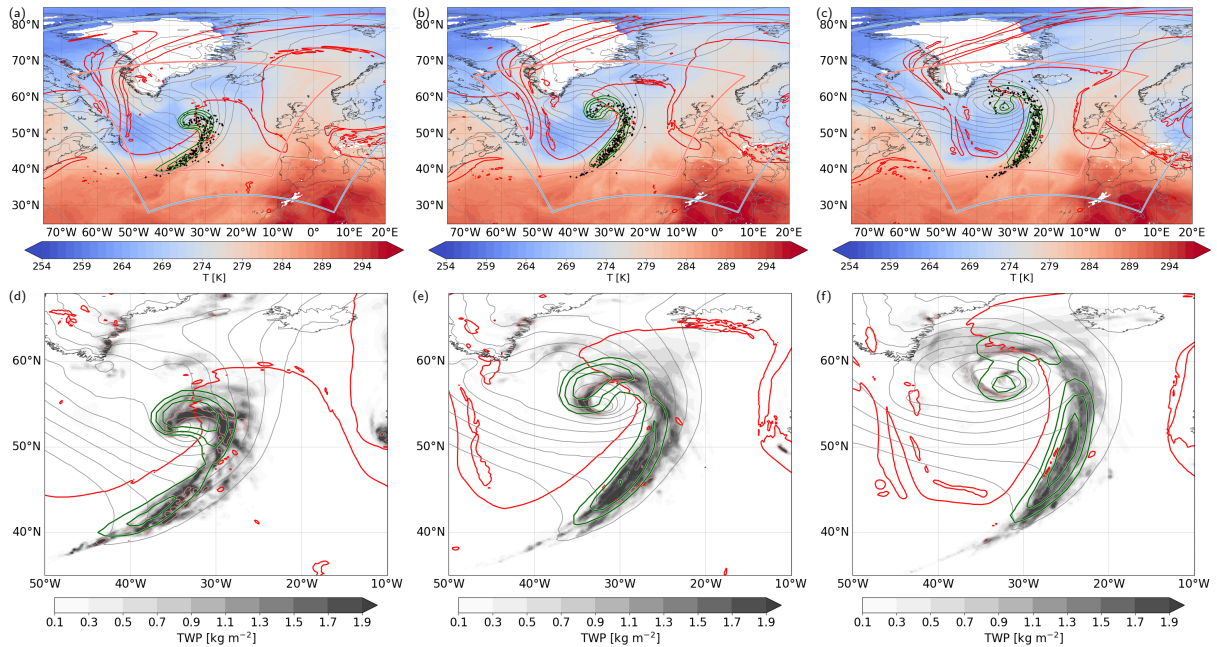
Figure 3. (a-c) Temperature at 850 hPa (shading, in K), SLP (grey contours, every 5 hPa), 2 PVU at 320 K isentrope (red contour), WCB ascent probability (at conditional probabilities of 0.3, 0.5, and 0.7, green contours), and online WCB trajectory positions for trajectories ascending at least 25 hPa in 2 h (black markers; only every 50th trajectory is shown) for **(a)** 12 UTC 4 Oct, **(b)** 18 UTC 4 Oct, **(c)** 00 UTC 5 Oct. The first and second refined nests are outlined in blue and red. **(d-f)** Total water path (TWP; shading, in kg m^{-2}) and graupel water path (pink contour, at 0.3 kg m^{-2}), SLP (grey contours, every 5 hPa), 2 PVU at 320 K isentrope (red contour), and WCB ascent probability (at conditional probabilities of 0.3, 0.5, and 0.7, green contours) for the same times as shown above. All data are from the R03B07 grid.

3 Case study introduction

The surface cyclone associated with the WCB initially develops on 02 Oct 2016 as weak SLP depression in a strong baroclinic zone east of 60°W at approximately 45°N and is associated with a local positive low-level PV anomaly. It propagates across the North Atlantic along the baroclinic zone at 45°N and has characteristics of a so-called diabatic Rossby wave (DRW, Boettcher and Wernli, 2013). On 03 Oct, the surface cyclone interacts with the approaching upper-level trough, intensifies further and develops clear warm and cold frontal structures. At this stage, the cyclone forms an extended cloud band which is associated with poleward directed WCB ascent, and subsequently propagates northward ahead of the upper-level trough. On 04 and 05 Oct, the WCB (represented by green contours in Fig. 3) ascends in the cyclone's warm sector ahead of the upper-level trough and into an amplifying ridge downstream (red contour in Fig. 3) which extends far north to 70°N. The ridge subsequently merged with a precursor ridge built-up by an intense precursor cyclone (Steinfeld et al., 2020; Flack et al., 2021) and contributed to the long-lasting block Thor (Maddison et al., 2019). Here, we focus on the period from 04-06 Oct when the WCB ascent is most pronounced and forms a large-scale cloud band (Fig. 3d-f).
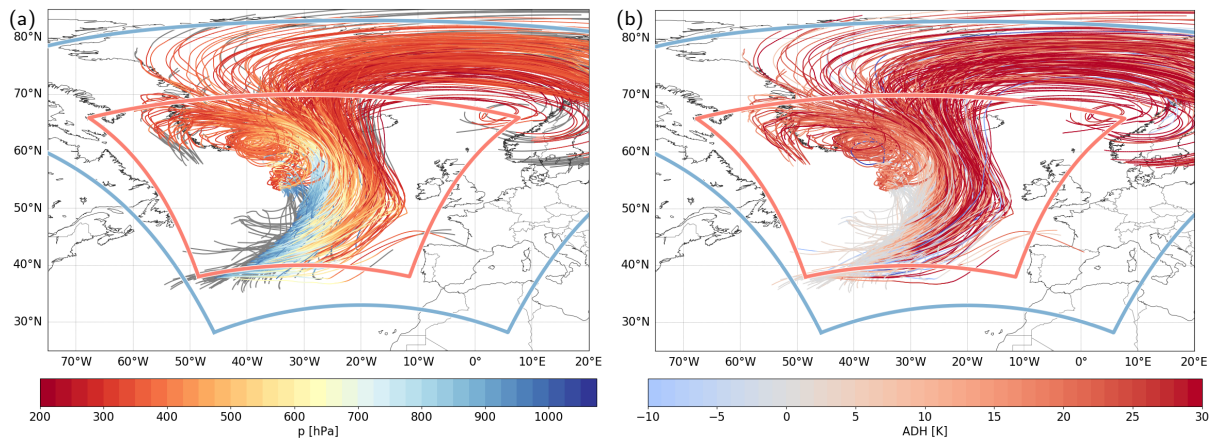
Figure 4. Online WCB trajectories starting their fastest 600 hPa ascent at 12 UTC 4 Oct coloured according to **(a)** pressure (p, in hPa) and **(b)** ascent integrated diabatic heating from all microphysical processes (ADH, in K). In **(a)** the WCB trajectory positions prior to the start of the fastest ascent, and after 48 h ascent time are shown in grey. The refined nests are outlined in blue and red.

Between 04 and 05 Oct, WCB air parcel locations, identified from online trajectories, ascend poleward in the warm sector of the cyclone ahead of the surface cold front, above the warm front, and near the cyclone center (black markers in Fig. 3a-c).
325 Their ascent is associated with the formation of an extended, dense cloud band (Fig. 3d-f) including the formation of graupel near the frontal regions in the early ascent phase (Fig. 3d). Although WCB trajectories spread out in the ridge once they reached the upper troposphere, the major ascending motion is confined to the near-frontal regions (Fig. 3a-c), where WCB ascent occurs primarily in a narrow and elongated, north-south oriented band. In general, the location of the ascending segment of the online WCB trajectories is well captured by the CNN-based WCB ascent diagnostic (green contours in Fig. 3a-c), which thus proves
330 useful for diagnosing footprints of WCB ascent from Eulerian data also in high-resolution simulations.

The ascent of the selected approximately 36 000 WCB trajectories predominantly takes place in the inner-most convection-permitting nest providing a high resolution for WCB trajectory computation (Figs. 3a-c and 4). Some WCB trajectories move into the highest resolution nest before or during their ascent (Fig. 4). Moreover, many trajectories leave the highest resolution nest once they reached the upper troposphere near the strong jet region. This emphasizes that the transfer of trajectories between
335 different nests is important, in particular if the upstream evolution and the downstream impact of WCB trajectories is of interest. During the transfer of the trajectories across the nest boundaries, no discontinuities in location or WCB trajectories' properties can be observed, which is illustrated exemplarily for the evolution of pressure (Fig. 4a) and integrated diabatic heating from all microphysical processes along WCB trajectories (Fig. 4b; see Section 4 for a detailed description of diabatic heating along WCB trajectories).
340 Figure 5 illustrates the vertical WCB cloud structure and hydrometeor distribution in West-East oriented vertical cross-section composites centred relative to the western boundary of the CNN-based WCB ascent region during two days of WCB ascent (see Section 2.6). WCB ascent (black contour in Fig. 5d) occurs in the warm sector ahead of the sloping cold front

(isentropes and temperature in Fig. 5 a) and upper-tropospheric trough (reflected in the reduced height of the dynamical 2-PVU tropopause, shading in Fig. 5 b), and is associated with a vertically-extended cloud (Fig. 5 c). The precipitating WCB cloud band, reflected in high values of total hydrometeor content (shading in Fig. 5c) extends from the surface to approximately 11 km height, and slopes towards the East into the upper-level ridge, which is characterized by an elevated tropopause height, warmer temperature and low upper-tropospheric PV values (Fig. 5a,b). Within the WCB cloud band, the 0°C-isotherm is located at approximately 3 km altitude, and the mixed-phase region of the cloud extends from approximately 2 km to 6 km (Fig. 5c). The presence of supercooled liquid water facilitates riming and graupel formation between 2-4 km altitude. The microphysical processes lead to a large net diabatic heating in the cloud, while below the cloud, microphysical processes are associated with a net cooling (Fig. 5d). Diabatic heating contributions from individual microphysical processes are discussed in Section 4. As expected, the cloud band coincides with ascending motion on the order of 0.01 to $0.08 \, \mathrm{m \, s^{-1}}$ averaged across all individual cross-sections, while the post-frontal region west of the cold front is characterized by descent (Fig. 5d). The vertical cross-section composites illustrate the general characteristics of the WCB cloud band and ascent region, however, the compositing technique hides the heterogeneity of WCB ascent behaviour and characteristics reported in previous studies (Oertel et al., 2019; Blanchard et al., 2020; Boettcher et al., 2021; Oertel et al., 2021) and which is evident in instantaneous cross-sections. The online trajectories enable a more detailed perspective of the individual processes and detailed WCB ascent behaviour.
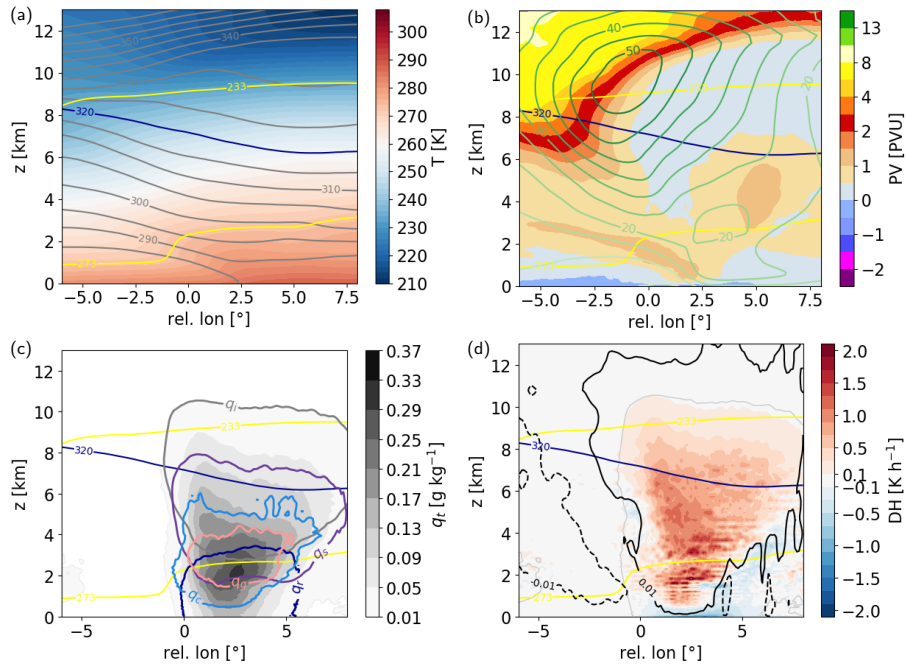
Figure 5. Vertical cross-section composites through the WCB ascent region ahead of the cold front for **(a)** temperature (T, in K), and potential temperature (every 5 K, grey lines), **(b)** potential vorticity (PV, in PVU) and wind speed (every 5 m s^{-1}), **(c)** total hydrometeor content (q_t, in g kg^{-1}; shading), and rain (q_r; blue contour, at 0.02 g kg^{-1}), cloud (q_c; light blue contour, at 0.02 g kg^{-1}), snow (q_s; purple contour, at 0.01 g kg^{-1}), ice (q_i; grey contour, at 0.01 g kg^{-1}), and graupel (q_g; pink contour, at 0.02 g kg^{-1}) water content, and **(d)** total microphysical diabatic heating rate (DH, in K h^{-1}), vertical velocity (black contours at -0.01 and 0.01 m s^{-1} and outline of WCB cloud (grey line, at q_t=0.01 g kg^{-1}). All panels show 273 and 233 K isotherms (yellow) and 320 K isentrope (blue).

4 Diabatic heating in the WCB

During the trajectories' 48-h ascent from on average 950 hPa to 300-400 hPa (Fig. 6a), they are heated diabatically by on average approximately 25 K (Fig. 6c) resulting in a cross-isentropic ascent from around 290 K to about 315 K (Fig. 6b). However, substantial variability in ascent behaviour and associated diabatic heating is present. The ascent timescale for 600 hP ascent (τ_{600}) exhibits a large variability, and includes both very rapid convective WCB ascent with timescales of a few hours, and slow and gradual WCB ascent (Fig. 7), which is hidden in the composite perspective. The frequency distribution of τ_{600} values shows that most WCB trajectories ascend 600 hPa in 20-30 h (Fig. 7a). Thus, the average trajectory ascent time scale is considerably lower than 48 h and amounts to on average 25 h, similar to WCB ascent time scales reported in previous high-resolution case studies (Rasp et al., 2016; Oertel et al., 2020, 2021; Blanchard et al., 2020). In general, the 600 hPa integrated diabatic heating ranges from 15 K to more than 35 K (Fig. 7a). The latter is only found in rapidly ascending, convective WCB trajectories. Due to the large variability of ascent rates, the entire set of WCB trajectories is stratified into three subsets according to their ascent timescale, which influences the average diabatic heating and detailed microphysical processes. In the following, fast ascent is characterized by τ_{600} values below 18 h (25th percentile), and slow and gradual ascent is characterized by τ_{600} values above 30 h (75th percentile). The intermediate subset includes all trajectories with τ_{600} values in between, and hence, comprises the largest number of trajectories (Fig. 7a). The mean evolution of the three subsets of WCB trajectories is shown in Fig. 6.

As on average the faster ascending trajectories are heated more strongly, they also reach higher isentropic surfaces (Figs. 7a, and 6b,c) than the slowly ascending trajectories, in line with previous case studies (Oertel et al., 2020, 2021). Despite the relationship between total diabatic heating and ascent time scale, there is still considerable variability per ascent time scale bin (Figs. 7a). Generally, the faster trajectories ascend and also reach the upper troposphere further south ahead of the upper-level trough (not shown).

Recent WCB case studies have highlighted that convective motion can be frequently embedded in the gradual WCB ascent (Rasp et al., 2016; Oertel et al., 2019, 2021; Blanchard et al., 2020, 2021). Yet, the total diabatic heating contribution of embedded convection in WCBs has remained unclear. Figures 7b shows the cumulative distribution of the relative heating contribution of trajectories binned into 1-h τ_{600} bins. For example, trajectories with a 600 hPa ascent time scale below 10 h contribute on average 10% to total diabatic heating in this case study (Fig. 7b), although their averaged diabatic heating is substantially larger (Fig. 7c) compared to trajectories with slower ascent time scales. For example, WCB trajectories with ascent time scales above 25 h are on average heated 10 K less but, due to their larger number, still contribute more than 43% to total heating (Fig. 7b). Selecting thresholds of τ_{600} of 3 h, 4 h and 7 h (the latter shows a sudden drop of mean ADH in this case study) for embedded 'convective' or rapid ascent results in contributions to the total heating of 1.4%, 2.1%, and 4.9%, respectively. Thus, although rapidly ascending WCB trajectories are heated significantly more than gradually ascending trajectories, their total diabatic heating contribution is relatively small due to the small fraction of embedded convection. Relative contributions may, however, be more relevant in other case studies that are characterized by a larger amount of embedded convection than this WCB (e.g., Oertel et al., 2021).
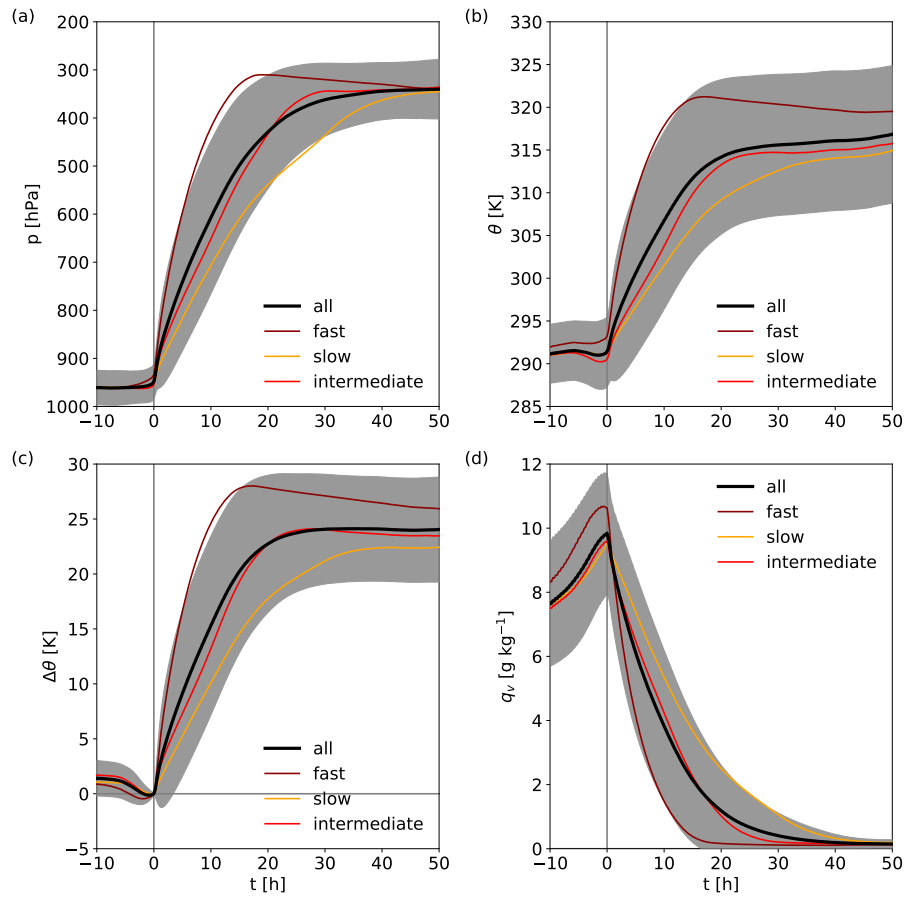
Figure 6. Mean evolution of **(a)** pressure (p, in hPa), **(b)** potential temperature (θ, in K), **(c)** accumulated change of potential temperature ($\Delta\theta$, in K), and **(d)** specific humidity (q_v, in g kg^{-1}) since start of fastest 600 hPa ascent phase for all WCB trajectories (black line, grey shading shows $\pm$ standard deviation), and for the fastest 25% (dark red), intermediate (red), and the slowest 25% (orange).
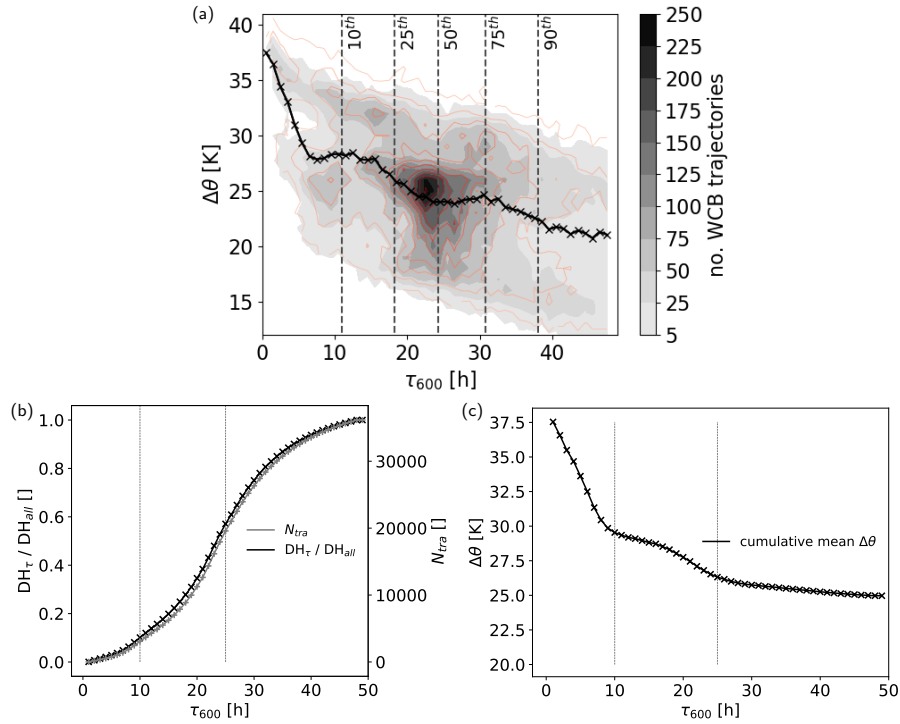
Figure 7. **(a)** 2D histogram of the duration of the fastest 600 hPa WCB ascent phases (τ_{600}, in h) and the change of potential temperature during this ascent phase ($\Delta\theta$, in K). Red contours show the maximum change of potential temperature along WCB trajectories. The black line and markers show mean diabatic heating per τ_{600} bin. Vertical lines show 10th, 25th, 50th, 75th, and 90th percentiles of τ_{600}. **(b+c)** Cumulative distributions of 600 hPa ascent integrated diabatic heating as function of τ_{600}. **(b)** Relative contribution to total diabatic heating (black) and WCB trajectory number (N_{tra}, grey), and **(c)** cumulative mean diabatic heating (black). The vertical lines are placed at τ_{600} = 10 h and τ_{600} = 25 h.

4.1 *ADH* from bulk physics processes

During their ascent, trajectories are heated and also cooled diabatically from a large variety of non-conservative processes, which together result in the large total diabatic heating discussed above. The mean integrated diabatic heating for individual physics processes at the end of each trajectories' 600 hPa ascent phase for fast, intermediate, and slowly ascending WCB trajectories is shown in Figure 8. On average, the total 600 hPa integrated heating ($\Delta\theta$) amounts to 25 K, whereby the fast WCB trajectories are heated 3.8 K more than the intermediate WCB trajectories, and 5.5 K more than the slowly ascending WCB trajectories (Fig. 8a).

The by far largest diabatic heating contribution results from microphysical processes (Figs. 8a). The evolution of *ADH* along WCB trajectories is shown in Fig. 9. During their ascent, WCB trajectories are rapidly heated through cloud formation, and after traversing through the mid-troposphere, the heating rate slows down (Fig. 9a-c). Turbulent diffusion, heating from the convection scheme (deep or shallow convection only, depending on the local resolution of the grid; see Section 2) and short-wave radiation also lead to a net heating of the trajectories during the ascent, while long-wave radiative cooling is important in particular when trajectories approach the cloud top (Fig. 9a-c and 8a). Diabatic heating from non-orographic and orographic gravity wave drag has a minor contribution and is, hence, not explicitly considered in the following.

Microphysical heating has by far the largest contribution to the total diabatic heating with on average 95% of total heating, and thus, substantially determines the cross-isentropic ascent of WCB trajectories. The larger total heating for fast WCB ascent compared to slow WCB ascent is strongly related to larger diabatic heating through microphysical processes (Fig. 8a). In contrast, prior to the ascent, when trajectories are located in the lower troposphere, they are markedly cooled by microphysical processes (Fig. 9a-c). Individual processes that contribute to the total microphysical heating are discussed in detail in the next section (Section 4.2).

In the lower troposphere, diabatic heating by turbulent diffusion is the second most important process associated with a net heating. Integrated over the entire 600 hPa ascent, net turbulent heating amounts to 1.4 K on average (Fig. 8a, and is slightly larger for fast WCB ascent (ADH_{TURB}=1.8 K) than for intermediate and slow WCB ascent (ADH_{TURB}=1.1 K and 1.6 K, respectively). The turbulent diffusion scheme is primarily active ahead of the approaching cold front in the warm sector between the surface and approximately 4 km height and forms a vertically oriented heating-cooling dipole (Fig. 10c, black solid and dashed contours). Gradient Richardson numbers are large in the WCB ascent region [1], and thus, a pronounced heating-cooling dipole was not expected, although a recent study by Wimmer et al. (2022, see their Figs. S3 and S4) also shows such a heating-cooling dipole below 600 hPa height in the WCB ascent region. We assume that the turbulent diffusion scheme reacts to the pronounced vertical heating from the first saturation adjustment (Fig. 10a) which is called before the turbulence scheme and instantly modifies the local temperature profile.

The average heating from the convection scheme is comparatively small and amounts to only 1.7% of total *ADH* (Figs. 8a and 9a-c), primarily because deep convection is treated explicitly in the inner-most nest, where most trajectories ascend. As outlined above, this does not imply that embedded convection is absent or irrelevant, as convective WCB ascent can be

---

[1]Only in the lowest 1 kilometer the gradient Richardson number drops below 1.

explicitly represented in the high-resolution nest. On average, ADH_{con} amounts to 0.5 K, and is smallest for the fast WCB
trajectories (0.3 K for fast ascent, compared to 0.5 K for intermediate, and 0.6 K for slow ascent). ADH_{con} is larger for the
more slowly ascending WCB trajectories as they remain longer in the lower troposphere, where the primary heating source
from the (shallow) convection scheme is located (Fig. 11e, black contour).

While shortwave radiation has a small heating contribution of on average 0.5 K during WCB ascent, long-wave radiation
substantially cools the ascending air near cloud top in the upper troposphere, and hence, reduces the isentropic outflow level
of WCB trajectories (Figs. 8a, 9a-c, and 11d). This upper-level cooling contribution is non-negligible and amounts to on
average -2 K integrated over the 600 hPa ascent. As the upper-level WCB cloud band can be relatively long-lived and the WCB
trajectories remain in the cloud for several hours, cloud top cooling continues to reduce potential temperature of the WCB air
parcels even after they have finished their main ascent.

4.2 ADH from individual microphysical processes

In the following, we discuss the heating contributions from the individual microphysical processes. Net microphysical heating
is dominated by condensation in the lower troposphere, which is realized by a first saturation adjustment, and leads to a rapid
warming at the onset of the WCB ascent (Figs. 8b, 9d-f). Condensation is strongest in the warm-phase region of the WCB as
reflected by the diabatic heating from the first saturation adjustment ahead of the cold front (Fig. 10a, black contour), however,
is also relevant in the mixed-phase region up to approximately 6 km height. In the upper troposphere, vapor deposition on frozen
hydrometeors takes over and dominates the subsequent cross-isentropic ascent (Fig. 10b, black contour; Fig. 9d-f). Together,
condensation (on average 17 K) and vapor deposition on frozen hydrometeors (on average 13 K) dominate the microphysical
heating budget (Figs. 8b, 9d-f), as expected from previous case studies (Joos and Wernli, 2012; Mazoyer et al., 2021). Vapor
deposition is additionally split into its contributions from deposition on ice, snow, and graupel plus hail, respectively. In total,
integrated heating from vapor deposition on ice ADH_{QIDEP} is largest with an average heating of 7 K along the ascent. It
also continues at higher altitudes and in lower temperature ranges where depositional growth of snow is small (Fig. 9d-f).
ADH_{QSDEP} amounts to on average 4 K, while vapor deposition on graupel ADH_{QGDEP} has the smallest contribution of on
average 1 K. The Eulerian perspective illustrates that the heating maximum of depositional growth of frozen hydrometeors is
located at around 6 km height (Fig. 10b, black contours). Although heating dominates along the ascending WCB trajectories,
the forward-sloping shape of the cloud band results in sublimation of sedimenting snow between 3-5 km height at the Eastern
edge of the cloud band. Cooling from sublimation also occurs in a small region above the cold front.

The initial riming process prior to the growth of rimed particles by vapor deposition is associated with an averaged heating
contribution of only 0.7 K (Fig. 8b), which is partially related to the small value of the specific latent heat of freezing, which is
released during riming. Riming takes place in the mixed-phase region of the cloud between 2-6 km height (Fig. 11a).

Another major contribution included in the microphysical budget is related to the second saturation adjustment, which is
associated with substantial cooling of an average 5 K during WCB ascent (Fig. 8b), and thus, reduces the heating from the
first saturation adjustment and vapor deposition. The second saturation adjustment forms a vertically oriented cooling-heating-
cooling tripole in the lowest 7 km (Fig. 10c, black contour), which leads to a non-monotonic $ADH_{satadII}$ evolution when

trajectories ascend through this region (Fig. 9e,f). The cooling from the second saturation adjustment results from an evapora-
tion of cloud droplets in sub-saturated conditions as a response to established non-equilibrium conditions from processes that
are called between the first and the second saturation adjustment (i.e., the turbulence scheme and all explicit microphysical
processes; see Section 2.2). The cooling-heating dipole below 4 km height is to a large extent a response of the saturation
adjustment to the turbulence scheme, which is characterized by a dipole of opposite sign (cf. Fig. 10c,d). Hence, to a large
extent, the diabatic heating and cooling from the second saturation adjustment in the warm phase can be understood as a
quasi-compensation of the heating dipole from the turbulence scheme which leads to sub- and super-saturated conditions and
ultimately the response of the second saturation adjustment (cf. discussion in Section 4.1). In contrast, the second saturation
adjustment's local cooling maximum in the mixed-phase cloud region above the 0°C-isotherm results to some extent from
the model representation of the Wegener-Bergeron-Findeisen process (Storelvmo and Tan, 2015), and reduces the substantial
heating from vapor deposition in the mixed-phase region (Fig. 10b,d).

Evaporation of rain and melting of ice hydrometeors that are sedimenting into ascending WCB air represent important
cooling processes. The total cooling through rain evaporation during the fastest 600 hPa ascent is relatively small and amounts
to 0.4 K on average (Fig. 8b), and can arise during embedded phases of trajectory descent. Evaporative cooling is indeed
important prior to the start of the WCB ascent, when trajectories are located in the inflow region in the lower troposphere below
the cloud band (Figs. 11b, 9d-f) where evaporative cooling dominates the total microphysical budget (Fig. 5d). Evaporative
cooling within 10 hours prior to the ascent amounts to on average 2 K (Fig. 9d-f), and thus, can play an important role for
the pre-conditioning of WCB air masses prior to their ascent. Melting from falling ice hydrometeors becomes important once
trajectories approach the 0°C-isotherm, where the maximum cooling through melting is located (Fig.11c, black contour).
Integrated along the WCB ascent, cooling from melting processes amounts to on average 1 K, and thus, has a comparable
magnitude to depositional growth of rimed particles (Fig. 8b). Overall, cooling from these processes offsets the strong heating
from primarily condensational growth and can reduce the isentropic outflow level by on average 6 K along the ascent.

The remaining microphysical processes explicitly represented in the two-moment scheme (CCN activation, freezing of cloud
and rain droplets, homogeneous, deposition and immersion nucleation, as well as evaporation from melting ice hydrometeors)
have comparably small heating contributions (Figs. 9g-i, 8c). Thus, in terms of total heating they are almost negligible, which
is primarily related to the small amount of mass conversion. Nevertheless, we hypothesize that the representation of these
processes is important, because they influence the number concentrations of liquid and frozen hydrometeors (cf. Fig. B1),
which subsequently influences the strength of other microphysical processes.

4.3 Relationship between WCB ascent behaviour and microphysical processes

Faster ascending trajectories are associated with larger ADH, which to a large extent results from stronger total microphysical
heating (Section 4.1, Figs. 7a, 8a). The latter is linked to on average larger initial moisture content of faster ascending WCB
trajectories, which represents a thermodynamic constraint on the total diabatic heating from microphysics along the WCB
airstream. A particularly large difference arises from the saturation adjustment. ADH_{SATADI} for quickly ascending trajecto-
ries is 5 K larger than for slowly ascending trajectories. In contrast, ADH_{QXDEP} differs less than 1 K between different ascent

categories. Hence, in this case study the larger cross-isentropic ascent of the faster ascending WCB trajectories is substantially driven by larger initial moisture content of the rapidly ascending WCB trajectories (Fig.6d), which is available for condensation. Considering the relative contributions of depositional growth of snow, ice, and graupel for the different WCB ascent categories additionally shows that for slower ascent vapor deposition on ice becomes increasingly more important. Prolonged residence time and enhanced hydrometeor growth in faster updrafts favours riming, thus, heating from particle riming and depositional growth of rimed particles is considerably larger for fast WCB ascent compared to slower WCB ascent (Fig. 8b). The representation of graupel in the WCB is relevant as total diabatic heating from riming and growth of rimed particles (i.e., QGDEP plus QXRIM) on average exceeds 2.5 K along fast ascending WCB trajectories. Besides the second saturation adjustment, melting of frozen hydrometeors and evaporation of rain have the largest microphysical cooling contributions during the ascent (Fig. 9d-f). Cooling contributions of evaporation and melting are both smaller for fast WCB ascent because WCB air parcels ascend faster through the relatively well-constraint vertical layers of the atmosphere where evaporation and melting are most pronounced (Fig. 11b,c, black contours). In contrast, the slower ascending WCB trajectories remain longer near the surface and near the melting level, where rain evaporation and melting are strongest (Fig. 11b,c, black contours). Thus, the slowly ascending WCB air parcels are not only heated less, but also experience enhanced cooling from below-cloud evaporation and melting.

In the following, we consider processes associated with smaller mass conversion and related diabatic heating (Figs. 9g-i and 8c). Counter-intuitively, ascent-integrated heating from activation of cloud droplets (Fig. 8c) is larger for slow ascent, although stronger updraft velocity is implicitly associated with larger supersaturation and an increase in CCN activation (eq. A1; Fig. 2). Indeed, the initial increase of ADH_{QCACT} is strongest along fast WCB trajectories, however, the prescribed activation rate of cloud droplets decreases quickly with altitude (Fig. 2). The larger ADH_{QCACT} for more slowly ascending WCB trajectories is attributed to the time integration as the slower WCB trajectories remain longer in the lower to mid-troposphere where CCN activation, as prescribed in the parameterisation, is most active (Fig. 2). The latter is probably entirely dependent on the CCN activation parameterisation, as no secondary CCN activation above cloud base would be expected at the typical evolution of updraft velocities along WCB ascent, which, however, is not accounted for in the ICON microphysics.

Freezing of cloud droplets and rain drops is more important during faster WCB ascent, as the timescale of transport in fast updrafts is smaller than the timescale of rain formation. Consequently more condensate is transported to colder temperatures and is available for freezing (Figs. 8c, 9g-i). In particular the homogeneous freezing of cloud droplets, which can produce large ice number concentrations, influences the cloud structure via changes to the ice crystal number concentration.

Homogeneous and heterogeneous freezing (immersion and deposition freezing) also have a negligible direct effect on the diabatic heating in the WCB due to the small mass conversion (Figs. 8c, 9g-i). Moreover, they mostly occur once WCB air parcels are finishing their main ascent. Evaporation from melting of frozen hydrometeors is associated with a small cooling of the ascending WCB air. Similarly to ADH_{QCACT}, the temporal integration accounting for the time trajectories spend in the region influenced by evaporative cooling is decisive for total ascent-integrated cooling.

In summary, shorter ascent timescales (i.e., faster ascent) are associated with larger heating from the first saturation adjustment, riming, and freezing of rain, in contrast to the relative contribution of vapor deposition which is reduced compared to longer ascent timescales (i.e., slower ascent). Simultaneously, long-wave radiative cooling, evaporative cooling and cooling from melting of frozen hydrometeors are reduced due to the shorter integration time scale. Vice versa, the slower WCB trajectories ascend, the less important is heating from the first saturation adjustment and riming, and the more important becomes heating in the ice phase from vapor deposition compared to the mean over all trajectories. The larger diabatic heating from microphysical processes for faster ascending trajectories is related to enhanced specific humidity at the start of the ascent, which provides a thermodynamic constraint and emphasizes the relevance of WCB inflow moisture for total diabatic heating from microphysical processes and WCB trajectories' cross-isentropic ascent.

The heterogeneity of WCB ascent behaviour is in line with previous results highlighting the heterogeneous cloud structure of the WCB and its embedded convection (e.g., Crespo and Posselt, 2016; Oertel et al., 2019; Gehring et al., 2020). We further find that the heterogeneity is influenced by different microphysical processes that influence the cloud structure, but also latent heating and cooling along the ascent, which finally determines the total cross-isentropic ascent. Detailed representation of these processes in high-resolution NWP simulations allows to represent some of the variability in the cloud structure of WCBs. The stratification according to ascent behaviour also emphasizes the relevance of WCB air parcels' residence time at a certain altitude for the total ascent integrated diabatic heating.
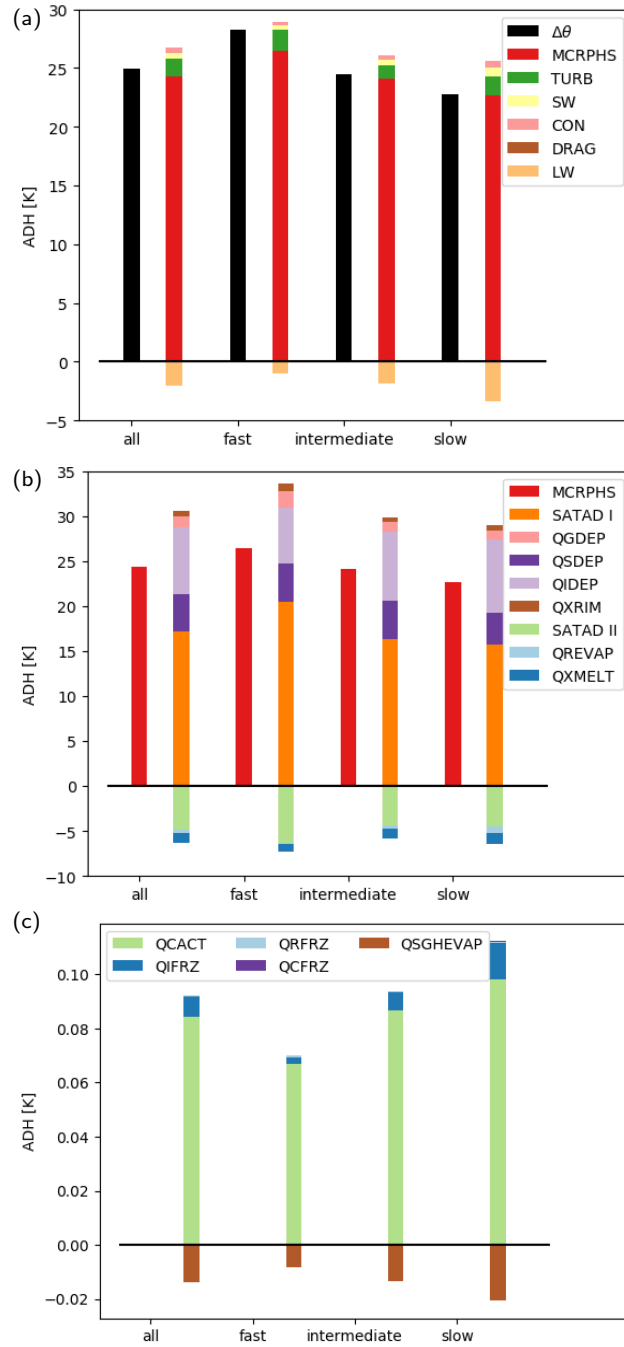
Figure 8. Mean $600\,\mathrm{hPa}$ ascent integrated diabatic heating (ADH, in K) for all WCB trajectories, and the fastest 25%, intermediate, and slowest 75% of all WCB trajectories for all processes shown in Fig. 9. **(a)** shows the net change of potential temperature ($\Delta\theta$) as well as ADH from MCRPHS, TURB, DRAG, LW, and SW. **(b)** shows ADH from MCRPHS, SATAD I and II, QSDEP, QIDEP, QGDEP, QXRIM, QREVAP, and QXMLT. **(c)** shows ADH from QSGHEVAP, QIFRZ, QCACT, QRFRZ, and QCFRZ.
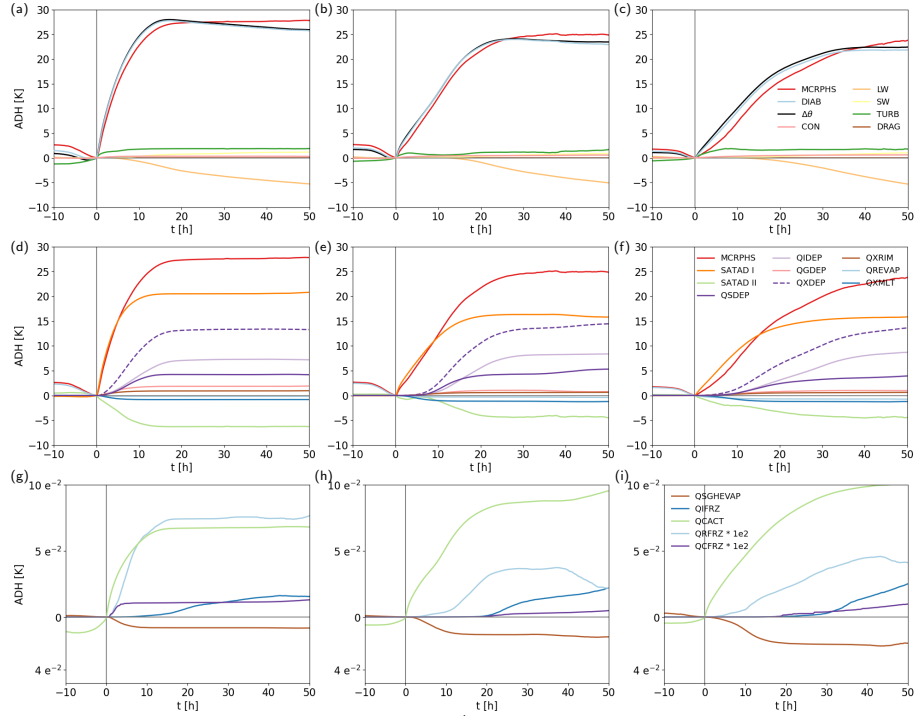
Figure 9. Mean evolution of accumulated diabatic heating (ADH, in K) along **(a,d,g)** fast, **(b,e,h)** intermediate and **(c,f,i)** slow WCB trajectories since start of the fastest $600\,\text{hPa}$ ascent phase (cf. Fig. 6). **(a-c)** shows ADH for turbulence (TURB), sub-grid scale orographic and graphity wave drag (DRAG), short- and longwave radiation (SW and LW), microphysics (MCRPHS), and the sum of all diabatic processes (DIAB), as well as the net change of potential temperature ($\Delta\theta$). **(d-f)** show ADH from first and second saturation adjustment (SATAD I and II), vapor deposition on snow, ice, graupel plus hail, and the respective sum (QSDEP, QIDEP, QGDEP, and QXDEP), riming (QXRIM), rain evaporation (QREVAP), and melting (QXMLT). **(g-i)** show ADH from evaporation from melting hydrometeors (QSGHEVAP), homogeneous and heterogeneous ice nucleation (QIFRZ), cloud droplet activation (QCACT), and freezing of rain (QRFRZ) and cloud droplets (QCFRZ). Note that QRFRZ and QCFRZ are scaled by 100.

5 Diabatic PV modification

5.1 Overview of diabatic PV changes

The strong ascent and diabatic heating of the WCB airstream typically results in low-level positive and upper-level negative PV anomalies (e.g., Madonna et al., 2014; Methven, 2015). Generally, the evolution of PV along the WCB trajectories (Fig. 12a-c) shows the well-known increase of PV during the first part of the ascent followed by a PV decrease later on (e.g. Wernli and Davies, 1997; Madonna et al., 2014; Joos and Wernli, 2012; Methven, 2015). On average, the WCB trajectories arrive in the upper troposphere near the tropopause with PV values below 0.5 PVU (Fig. 12a-c). The PV evolution along the ascent-centred trajectories shows a strong local maximum of 1-1.5 PVU immediately after the start of the ascent, which quickly decreases before reaching a plateau phase that is more pronounced for the intermediate and slowly ascending WCB trajectories and followed by further PV decrease. The initial PV increase along the ascent is much more rapid than shown in previous studies (e.g., Madonna et al., 2014; Joos and Wernli, 2012; Martínez-Alvarado et al., 2014), emphasizing the pronounced PV production in the lower-most 1 km (Fig. 11f; cf. Fig. 5b) and its subsequent re-distribution. The strong initial PV increase is likely emphasized by centering the trajectories relative to the start of their fastest 600 hPa ascent and/or may be model and case dependent.

Integrating the PV tendencies from selected individual physics processes along the trajectories (APV) shows their contribution to the total change of PV (Fig. 12). The integrated effect of all diabatic PV tendencies (APV_{DIAB}, Fig. 12; neglecting PV change from momentum tendencies) approximately follows the evolution of total PV. The integrated effect of all microphysical processes only (APV_{MCRPH}) is responsible for the rapid PV increase in the lower troposphere, and also results in a subsequent decrease of PV. However, PV reduction is underestimated if the PV tendency from turbulent heat transfer is neglected (cf. $APV(\sum DIAB)$ and $APV(\sum MCRPH)$ in Fig. 12a-c and APV_{TURB} in Fig. 12d-f).

Furthermore, differences between APV_{DIAB} and the PV evolution partially result from neglecting the momentum tendencies (e.g. Spreitzer et al., 2019; Rivière et al., 2021), which can be important in the lower troposphere (Stoelinga, 1996; Attinger et al., 2021) and near the jet (Spreitzer et al., 2019). Further, the computation of PV tendencies on the original high-resolution ICON grid can result in very large tendencies as locally large diabatic heating gradients can occur in the simulation (see also Rivière et al., 2021). These artificially large tendencies are interpolated to the trajectory positions and can degrade the total PV budget (cf. Rivière et al., 2021; Wimmer et al., 2022). This in particular applies to the PV tendencies from turbulence and the second saturation adjustment, which can take locally very high instantaneous values.

5.2 Contributions from individual diabatic processes

Similarly to the diabatic heating contributions, the largest PV modifications along WCB ascent result from both saturation adjustments, vapor deposition, and turbulent diabatic heating (Fig. 12d-f). Moreover, PV modification from rain evaporation also substantially contributes to an increase in WCB trajectories' PV values. Melting, riming, and radiative processes, as well as diabatic heating from the convection scheme contribute less to PV modification in the WCB.

APV from the first saturation adjustment, vapor deposition and riming are characterized by the characteristic positive and subsequently negative PV rates (Fig. 12d-f), as the WCB trajectories pass through the respective local heating maxima and the related vertical dipoles of PV production and reduction (Figs. 10a,b and 11a). The increase of APV_{SATADI} at cloud base is very sudden and pronounced. Its local maximum of PV production in the lower troposphere results from strong vertical gradients of diabatic heating below 1 km height that occurs in an environment with large cyclonic vertical vorticity (Fig. 10a), which strengthens the diabatic PV production. Above 1 km height and above the local heating maximum, PV is reduced. The magnitude of PV reduction is smaller than PV production in the lower-most troposphere, but has a larger vertical extent.

Evaporation of rain strongly cools the boundary layer and lower troposphere below cloud base. The low-level cooling results in PV production close to the surface, and at 1 km and 2 km height (Fig. 11b). Thus, APV_{QREVAP} along trajectories increases considerably, with the largest increase of PV prior to the ascent when WCB trajectories are located in the lower-most troposphere (Fig. 9d-f). In total, PV increase from evaporative cooling along the WCB trajectories amounts to approximately 0.5-0.7 PVU. Hence, evaporative cooling has a substantial contribution to the PV maximum along WCB ascent and to the lower tropospheric positive PV anomaly.

PV modification from vapor deposition is important between 3-9 km height. The net PV change from vapor deposition along WCB trajectories is approximately 0 PVU. Figure 10b shows the formation of a slightly tilted PV rate dipole, whereby PV reduction is stronger near the jet-facing side (eq. 3). Its formation results from horizontal heating gradients in a vertically sheared environment below the strong upper-level jet (Harvey et al., 2020; Oertel et al., 2020). Reduction of PV near the jet region enhances the negative PV anomaly, and contributes to the PV gradient across the tropopause.

Similarly to their respective heating rates, the PV rates of the second saturation adjustment and turbulence partially counteract each other, in particular below the 0°C isotherm. Due to locally large spatial heating gradients, the associated PV rates are very patchy and can take locally very large values (Fig. 10c,d) which influences the mean APV evolution along trajectories and can introduce interpolation errors. The vertically alternating patterns of strong PV reduction and production from the second saturation adjustment and turbulence (Fig. 10c,d) result from the vertical tripole of $ADH_{SATADII}$ and dipole of ADH_{TURB}, respectively (Section 4.1). These PV rate pattern are to some extent reflected along the ascending WCB trajectories (Fig. 12d-f), which, as mentioned above, additionally include interpolation errors and can be influenced from locally high values. Although both SATAD II and TURB are associated with very large individual PV rates, their combined effect, and thus, their feedback to the dynamical core is limited, as these processes to some extent compensate each other. Hence, we recommend that detailed process studies using the ICON model consider the combined effect of $TURB$ and $SATADII$ if total microphysical heating budgets, including the second saturation adjustment, are considered.

The PV rates from the other microphysical processes are substantially smaller, as their associated spatial heating gradients are smaller. Similar to APV_{QXDEP}, APV_{QXRIM} forms a vertical dipole of PV production and reduction, albeit with a smaller magnitude (Figs. 9d-f, 11a). As the diabatic heating maximum from riming is located near the 0°C isotherm, PV production and reduction takes place just below and above the melting level, respectively (Fig. 11a). In this region around the 0°C isotherm, the cooling maximum from melting of frozen hydrometeors is associated with PV reduction below 2 km height, and PV production above (Fig. 11c). Accordingly, APV_{QRMLT} decreases along WCB trajectories before it increases as trajectories pass through

the melting minimum. The net PV change along the ascent is approximately $0\,\mathrm{PVU}$, and the magnitude of APV_{QRMLT} is larger than PV modification from riming.

The heating tendencies from the remaining non-microphysical parameterisation schemes are also associated with small PV rates. As diabatic heating from the convection scheme is small (Section 4), the associated APV_{CON} is also comparatively small (Fig. 12). The convective heating in the boundary layer forms a low-level vertical dipole of PV production and reduction (Fig. 11e). Long-wave radiative cooling near cloud top and the associated PV rate dipole in the WCB ascent region are largest between 8-11 km height (Fig. 11d). The negative PVR below the long-wave cooling maximum overlaps with the negative PVR from vapor deposition, and together contribute to low PV values in the upper troposphere. While ADH_{LW} continuously decreases once WCB trajectories approach cloud top, APV_{RAD} depends on the WCB ascent behaviour and outflow height relative to cloud top. Fast WCB trajectories also reach higher altitudes and traverse the cloud top cooling minimum, resulting in initial PV reduction below and PV production above the cooling maximum, respectively (Fig. 9d-f). The more slowly ascending WCB trajectories remain below the cloud top cooling maximum. Thus, APV_{RAD} continuously decreases along their ascent.

In the cold sector of the cyclone (at relative longitude -3° to -6°), isolated shallow cumulus clouds form with cloud tops between 1-3 km height (Fig. 11d). Radiative cooling by these shallow cumuli is one of the most important factors for PV change in the cold sector and contributes to the low PV values at low altitudes. Near the surface PVR_{RAD} is negative in the cold sector and contributes to the negative near-surface PV values (Fig. 5b). PVR from radiative cooling is partially compensated by opposing PV tendencies from the shallow convection scheme (Fig. 11e), which is active in the cold sector and forms a PV tendency dipole near the 0°C isotherm. These processes are not directly relevant for the considered WCB, however, the pre-conditioning of the lower troposphere can influence potential successor cyclones and their WCBs (Papritz et al., 2021).

5.3 Summary of diabatic PV changes

In summary, the different physics processes considerably modify PV during WCB ascent. While the evolution of PV along WCB trajectories is generally described as sequence of PV increase followed by PV decrease as trajectories pass through the heating maximum (e.g. Wernli and Davies, 1997; Madonna et al., 2014), our detailed analysis illustrates the complicated interplay and differing, partially opposing, contributions of all physics processes to the overall evolution of PV. The ascent-centred Lagrangian perspective as well as the Eulerian composites emphasize the strong PV production in the lower-most troposphere by condensation and rain evaporation before PV values along the ascending WCB air parcels are reduced and eventually approximately approach their inflow values. PV reduction in the mid- to upper troposphere primarily results from condensation, vapor deposition, and longwave radiative cooling. Thereby, the PV evolution along the trajectories is influenced by the trajectories' ascent behaviour, i.e., the time the individual trajectories remain in regions which are predominantly influenced by either PV production or reduction.
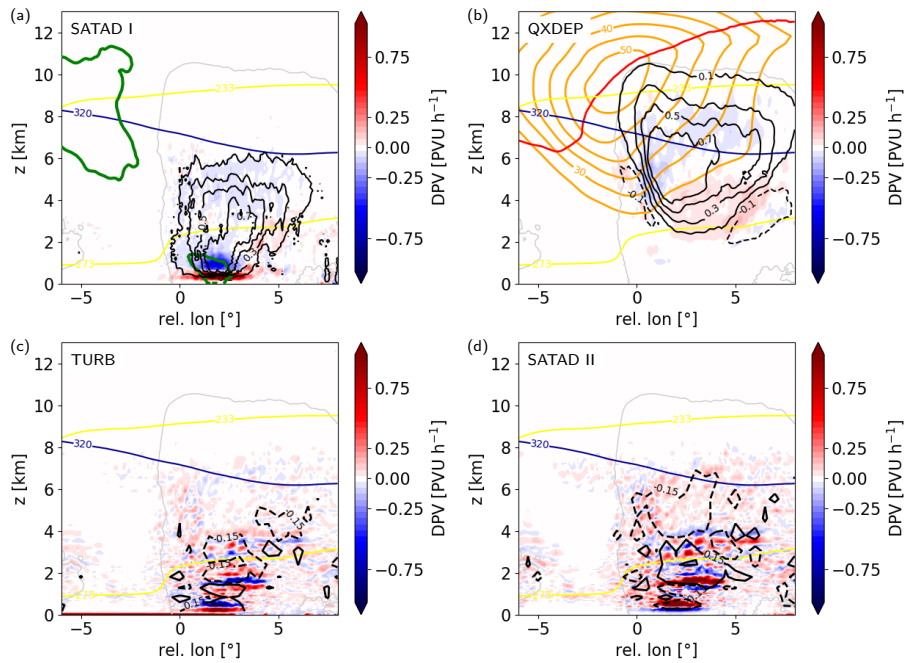
Figure 10. Vertical cross-section composites through the WCB ascent region ahead of the cold front for PV rates (PVR, in PVU h^{-1} in colours) and diabatic heating rates (black, in K h^{-1}) from **(a)** first saturation adjustment (SATAD I), **(b)** total vapor deposition (QXDEP), **(c)** turbulent temperature tendency (TURB), and **(d)** second saturation adjustment (SATAD II). Also shown are **(a)** vertical vorticity (green line, at 10^{-4} s^{-1}), and **(b)** wind speed (orange, every 5 m s) and the dynamical 2-PVU tropopause (red). All panels show 273 and 233 K isotherms (yellow), 320 K isentrope (blue), and the cloudy region (grey line, at q_t=0.01 g k^{-1}). Note that diabatic heating in **(c)** and **(d)** is interpolated to a coarser resolution for visualization of regions dominated by heating or cooling due the patchiness of the respective diabatic heating rates.
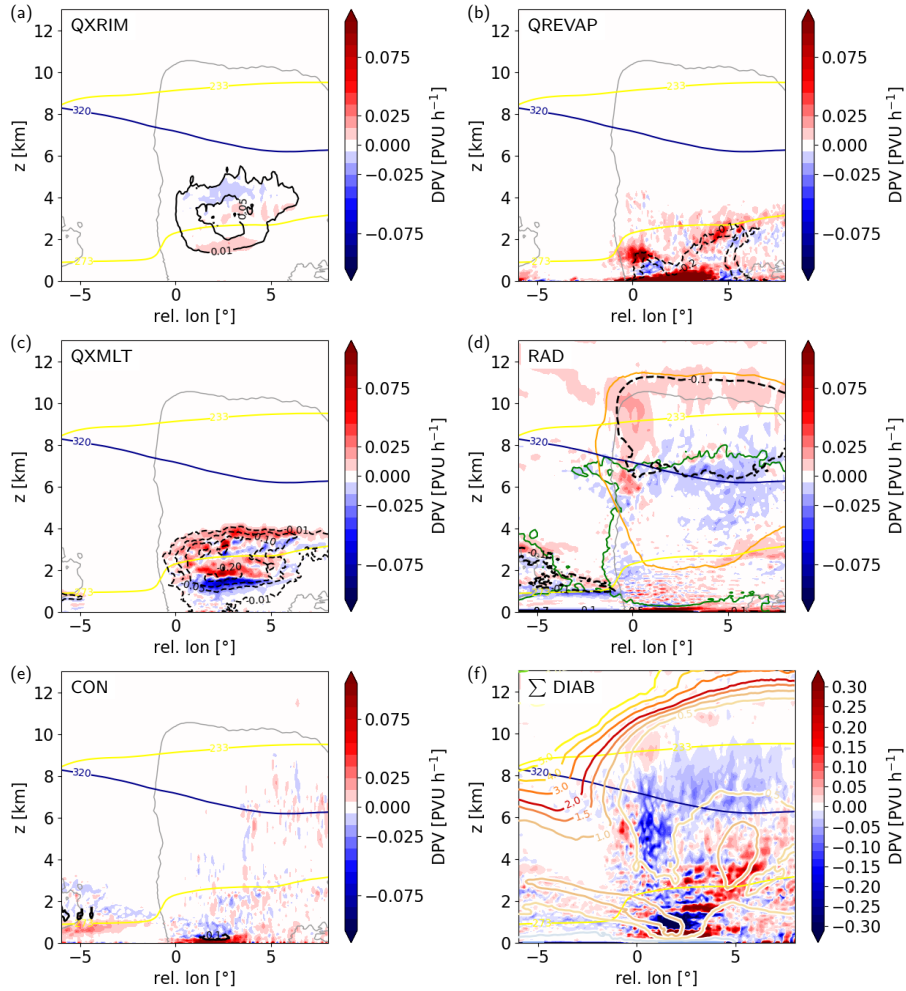
Figure 11. As Figure 10 but for **(a)** riming (QXRIM), **(b)** evaporation of rain (QREVAP), **(c)** melting (QXMLT), **(d)** sum of long- and shortwave radiation (RAD), **(e)** convection scheme (CON), and **(f)** sum of PV tendencies from all considered diabatic heating processes. **(d)** also outlines cloud and ice water content (green and orange contours, at $2\,mg\,kg^{1}$), and **(f)** includes the potential vorticity distribution (colored contours, in PVU). All panels show 273 and 233 K isotherms (yellow), 320 K isentrope (blue), and the cloudy region (q_t=0.01 g k^{-1}, grey line). Note that PV tendencies in **(a-e)** are one order of magnitude lower than those in Fig. 10.
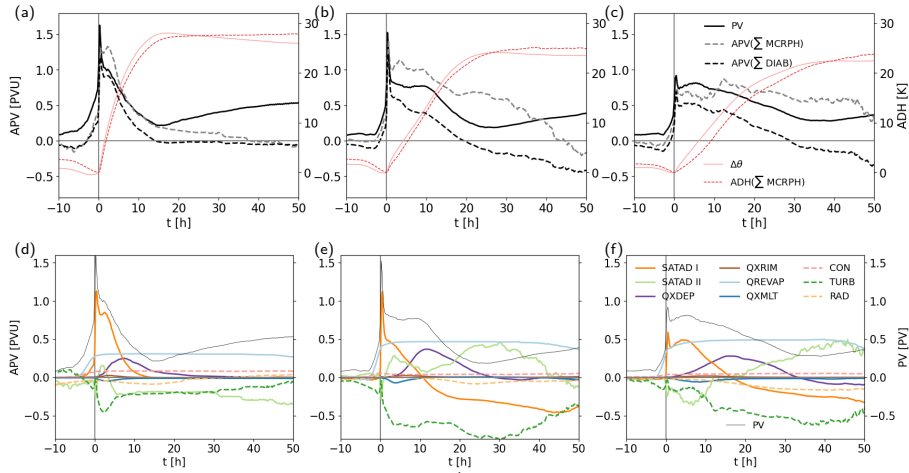
Figure 12. Mean evolution of PV and accumulated diabatic PV rates (APV, in PVU) along **(a,d)** fast, **(b,e)** intermediate and **(c,f)** slow WCB trajectories centred at the start of the fastest 600 hPa ascent phase (cf. Fig. 6). **(a-c)** PV as well as APV for relevant microphysical processes ($\sum$MCRPHS; SATAD I and II, QXDEP, QXMLT, QXRIM, and QREVAP), as well as microphysics plus TURB, CON, and RAD ($\sum$DIAB). Accumulated diabatic heating (ADH, in K) from all microphysial processes (blue dashed) and the net change of potential temperature (red, $\Delta\theta$) are shown on the secondary axis. **(d-f)** APV from individual non-conservative processes: SATAD I and II, QXDEP, QXRIM, QREVAP, QXMLT, CON, TURB, and RAD. Full PV is shown on the secondary axis.
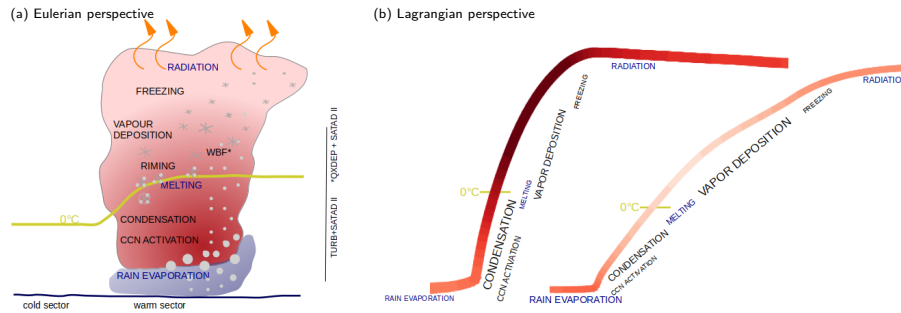
Figure 13. Schematic **(a)** Eulerian and **(b)** Lagrangian perspectives of non-conservative processes in a WCB represented by the ICON model. Additionally, **(a)** indicates the Wegener-Bergeron-Findeisen process (WBF) which is represented through the interaction of vapor deposition (QXDEP) and the second saturation adjustment (SATAD II) as well as the quasi-compensation of SATAD II and the turbulent temperature tendencies (TURB) in the lower troposphere. **(b)** The colors along fast and slow ascent indicate the respective ascent-integrated diabatic heating anomalies and the font size indicates the diabatic heating strength of the individual microphysical processes. The 0°C isotherm is slightly elevated along fast WCB ascent.

6   Concluding discussion

This study quantifies the individual diabatic heating contributions that determine the cross-isentropic WCB ascent using online trajectories in a two-way nested ICON simulation of a case study in the North Atlantic, and discusses the resultant diabatic PV modification. We provide a detailed ICON model perspective of microphysical process that are active in the WCB airstream and thus influence WCB ascent, cloud and precipitation structure. In addition to improved process and model understanding this lays the foundation for subsequent sensitivity experiments on the role of microphysical uncertainty for WCB ascent.

To account for reduced aerosol loading in the North Atlantic compared to continental regions, the ICON simulations were performed with a modified CCN activation scheme. The newly implemented nesting support for online trajectories allows the flexibility to use higher resolution nesting without being too limited in terms of the size of the refined area, which is particularly important for larger-scale systems, such as WCBs. In addition to quantifying the dominant (micro-)physical heating contributions for this WCB case study, we present complementary Lagrangian and Eulerian perspectives, that illustrate diabatic heating contributions (Fig. 13) as well as the interaction between detailed non-conservative processes and their effect on the PV distribution. The established Lagrangian perspective (e.g. Joos and Wernli, 2012; Joos and Forbes, 2016; Mazoyer et al., 2021) allows the quantification of processes that dominate the heat transport into the upper troposphere, and hence, determine the isentropic outflow level of the WCB airstream (Fig. 13b). The complementary Eulerian perspective based on WCB centred composites of vertical cross-section gives an overview of where the most important diabatic heating takes place (Fig. 13a) and how this modifies the PV distribution.

In agreement with previous case studies (Rasp et al., 2016; Oertel et al., 2019, 2021), we find a large heterogeneity in the WCB ascent behaviour, which not only affects the total ascent-integrated diabatic heating but also the heating contributions from individual (micro-)physics processes. The fast or convectively ascending WCB trajectories are on average heated sub-

stantially more than more gradually ascending trajectories, and thus, also reach a higher isentropic surface. However, their total heating contribution is still relatively small due to the small percentage of rapidly ascending WCB trajectories in this case study.

Consideration of all parameterised non-conservative processes shows that the ascent-integrated diabatic heating is dominated by microphysics with smaller contributions from turbulent processes and (shallow) convection. Long-wave radiative cooling near cloud top decreases the trajectories' isentropic level after their ascent.

From all microphysical processes, the first saturation adjustment, i.e. condensational growth of cloud droplets, and vapor deposition on frozen hydrometeors dominate the total heating in the lower and upper troposphere, respectively, which is in agreement with previous case studies (Joos and Wernli, 2012; Martínez-Alvarado et al., 2014; Mazoyer et al., 2021). Riming only has a small diabatic heating contribution, due to the small latent heat of freezing. During ascent, the WCB air is cooled by melting of sedimenting frozen hydrometeors near the 0°C isotherm. Evaporation of rain in the lower troposphere substantially cools the WCB air, in particular prior to WCB trajectory ascent. Integrated over the WCB ascent, the second saturation adjustment, that is called after the explicit microphysical processes, contributes to a cooling. In the mixed-phase region, it is associated with the Wegener-Bergeron-Findeisen process and evaporates cloud droplets after vapor deposition on frozen hydrometeors. Moreover, the diabatic heating tendencies from turbulent diffusion and the second saturation adjustment to a large extent compensate each other in the lower troposphere. Hence, we suggest that if diabatic heating from the second saturation adjustment is included in any microphysics budgets, the counteracting effects between turbulent diffusion and second saturation adjustment should be additionally considered, in particular, because the individual heating tendencies of both processes locally can be very large, but tend to counteract each other. The remaining microphysical processes that are explicitly represented in ICON's two-moment scheme (such as freezing and activation of cloud droplets) have negligible heating contributions, mainly due to small mass conversion. Although this has not yet been analysed systematically, we hypothesize that assumptions about the representation of these processes are still relevant, as they may to some extent influence processes with major diabatic heating contributions, such as vapor deposition, rain evaporation, or radiation, and due to their relevance for precipitation formation. For example, the modifications to the CCN activation scheme (Section 2.3), suggest that changes in CCN concentration slightly modify averaged heating rate profiles (Fig. B1d), and more strongly influence hydrometeor mass and number concentration distributions (Fig. B1a,b). Previous studies using coarser-resolution numerical models and including observations (Joos et al., 2017; McCoy et al., 2018) found some impacts of aerosol concentrations on WCB related precipitation and cloud structure. Mazoyer et al. (2021) reported only a minor impact of changing CCN concentrations on the entire simulation of a WCB case. Future studies should more systematically analyse the influence of CCN activation on microphysical processes, cloud and precipitation formation, and cloud-radiation interactions in WCBs, similar to impact studies of aerosol concentrations in convective environments (e.g., Seifert and Beheng, 2006b; van den Heever et al., 2011; Barthlott et al., 2017; Marinescu et al., 2021; Barthlott and Hoose, 2018; Barthlott et al., 2022).

While the detailed diabatic heating contributions, in particular from individual microphysical process rates, are model specific and vary depending on the parameterisation scheme (Joos and Forbes, 2016; Mazoyer et al., 2021; Wimmer et al., 2022), several studies using different WCB case studies, models and parameterisation schemes, have consistently suggested that

heating from condensation and vapor deposition are the dominant processes (Joos and Wernli, 2012; Joos and Forbes, 2016; Mazoyer et al., 2021). Therefore, we also expect that diabatic heating in other WCB case studies, which typically occur in an environment with strong dynamic forcing, is primarily determined by thermodynamic constraints. Thus, in future climate conditions the increase in specific humidity in the WCB inflow will results in enhanced diabatic heating and a higher outflow level (Joos et al., 2023).

We further analyse which PV tendencies strongly contribute to low-level PV production and upper-level PV reduction in the WCB. A local maximum of PV production is located in the lower-most troposphere, which is related to strong vertical gradients of the initial saturation adjustment in an environment with large vertical vorticity. Prior to the ascent, evaporation of rain near the surface also substantially contributes to PV production near the surface. These large positive near-surface PV values are transported upward by the ascending WCB before the air parcels' PV values decrease towards their initially low PV values due to PV reduction from condensation, vapor deposition, and longwave radiative cooling. Large integrated PV tendencies result also from the second saturation adjustment and heating from turbulence scheme. However, similar to their diabatic heating rates, the PV tendencies to some extent compensate each other, and on average contribute to a PV reduction although the detailed PV evolution should be considered with care due to interpolation errors of the locally large values. The additional microphysical processes such as evaporation, riming, and melting have smaller but non-negligible contributions to PV modification due to their smaller diabatic heating rates and resulting smaller heating gradients. The relative contributions of the physics processes to the overall PV evolution depend on the detailed model representation of cloud and other physics processes and are therefore probably model-dependent.

The model representation of microphysical processes, in particular assumptions about aerosol concentrations or ice microphysics, is associated with large uncertainties. It is still not clear how sensitive WCB ascent and the associated cloud structure and precipitation formation are to the detailed representation of individual microphysical parameters, and how such uncertainties propagate to the larger-scale. For example, it is yet open if environmental conditions, such as air pollution or dust outbreaks modifying CCN and IN concentrations, influence WCB ascent, or if the total ascent is insensitive to the detailed representation of cloud formation, as the bulk heating is dominated by the total conversion of specific humidity and therefore thermodynamic constraints. Therefore, sensitivity experiments employing the presented analysis framework will be conducted in future work, using varying assumptions about uncertain key parameters for WCB ascent. Such experiments can reveal if, and how, uncertainties in the microphysics parameterisations influence WCB ascent behaviour, integrated-diabatic heating and propagate to the larger-scale flow. Additionally, extending the analysis to further case studies, and to different microphysics schemes and NWP models, would shed more light into the role of detailed representation of individual microphysical processes for WCB ascent, the cloud structure, and associated precipitation characteristics.

Code and data availability. The ICON source code is distributed under an institutional license issued by the German Weather Service (DWD). For more information see https://code.mpimet.mpg.de/projects/iconpublic (DWD, 2015). The model output of the ICON simulation is available from the authors upon request. The vertical cross-section composites and WCB trajectory data will be accessible through

the public KITOpenData repository https://doi.org/10.5445/IR/1000159000 upon acceptance of this manuscript. Information and the source code for the convolutional neural networks model ELIAS 2.0 are available from Quinting and Grams (2022). Size-binned aerosol number

730 concentrations for the British FAAM flights during NAWDEX are available from the Centre for Environmental Data Analysis (CEDA) archive (CEDA, Centre for Environmental Data Analysis, 2016).

Appendix A: CCN activation

The CCN activation scheme (Hande et al., 2016) for the ICON-DE domain is optimized for aerosol number concentrations over Germany and based on extensive simulations and measurements of aerosol size distributions during the HD(CP)[2] Observational Prototype Experiment (HOPE) field campaign. The CCN activation is parameterised as function of updraft velocity and pressure, accounting for thermodynamic conditions and vertical distributions of aerosols, respectively (Fig. 2). Generally, the CCN concentration is high in the boundary layer and strongly decreases above.

Aerosol number concentrations over continental regions can differ substantially from concentrations over the open ocean. Previous studies showed that aerosol number concentrations over ocean decrease less strongly with height than over continental regions, especially in the lower troposphere (Hudson and Xie, 1999; Wang et al., 2021), although variability in aerosol amount and its vertical distribution is large and, among others, varies with season and synoptic conditions. The modified CCN activation parameterisation takes the substantially differing aerosol characteristics over the North Atlantic compared to continental Germany into account and is based on airborne measurements of size-resolved aerosol number concentrations from three research flights of the British Facility for Airborne Atmospheric Measurements (FAAM) BAe 146 that took place during the NAWDEX campaign in September and October 2016 (CEDA, Facility for Airborne Atmospheric Measurements; Natural Environment Research Council; Met Office, 2016a, b, c; CEDA, Centre for Environmental Data Analysis, 2016). Size-binned aerosol number concentrations were measured with a Passive Cavity Aerosol Spectrometer Probe (PCASP) in the range of $0.2\,\mu$m to $3\,\mu$m (Nott, 2013; Droplet Measurement Technologies, 2017). The individual steps for the modification of the CCN activation scheme are outlined below.

Observations

The FAAM aircraft operated from the United Kingdom (UK), and measurements were taken to the West and North of the UK over the Atlantic and Scotland (Fig. A1a). To account for air mass origin of PCASP measurements, 24-h backward trajectories were calculated with LAGRANTO (Sprenger and Wernli, 2015) from 3-h ERA5 reanalysis data (Hersbach et al., 2019, 2020). Trajectories were started in the region around the flight tracks and every $100\,$hPa in the vertical. The backward trajectories show that the flights in September were influenced by long-range transport of maritime air advected from the North Atlantic during the transition to and presence of a zonal weather regime (Schäfler et al., 2018; Grams et al., 2017), while air measured during the October flight is potentially more strongly influenced by continental aerosol concentrations with low-level and mid-level air masses advected from the North Sea region during a Scandinavian blocking (Fig. A1a).

PCASP measurements with a temporal resolution of $1\,$s are available. Data during strong sinking or rising flight segments was removed, which substantially reduced the number of available data (Fig. A1b). 10-minute along-flight averages were calculated prior to computing the median size distribution (dN/dln(D)) for the marine boundary layer (MBL) and the free troposphere (FT), separately (Fig. A1c). Both aerosol size distributions show two local maxima, hence, two log-normal aerosol size distributions for the accumulation and the coarse mode were fitted (Fig. A1c).

Cloud parcel model simulations

To obtain activated cloud droplet number concentrations based on the observed aerosol population, we conduct parcel model simulation with *pyrcel* (Rothenberg and Wang, 2016), which due to a very short time step allow to explicitly predict the supersaturation evolution. The latter is key for CCN activation and is not represented in ICON. Parcel model simulations use the fitted aerosol size distributions assuming ammonium sulfate for the accumulation mode and sea salt for the coarse mode (note that results are not very sensitive to these assumptions). Simulations were started at different pressure values (1000 hPa - 400 hPa) with constant vertical velocities of ($0.01\,\mathrm{m\,s^{-1}}$ to $50\,\mathrm{m\,s^{-1}}$). Initial temperature values for the parcel simulations follow a dry adiabatic temperature profile and initial relative humidity is set to 99%. Parcel model simulations are computed for 3000 s. From each parcel model simulation the cloud droplet number concentration (CDNC) after the activation event, i.e. after reaching the maximum supersaturation, is retrieved.

Parameterisation for CCN activation

The resulting CDNC values were used to fit a parameterisation for CCN activation depending on pressure and vertical velocity (eq. A1), similar to the CCN activation scheme developed by Hande et al. (2016, Fig. 2). The aerosol number concentration N_a is assumed to be quasi constant in the well-mixed boundary layer, and to decay exponentially above with a scale height of 150 hPa for the accumulation mode and 400 hPa for the coarse mode (Fig. 2, eq. A1). The following equation describes the number concentration of activated cloud droplets N_c as function of vertical velocity w and pressure p:

$$N_c(w,p) = N_a(p) \cdot \left(1 + e^{-B(p) \cdot ln(w) - C(p)}\right)^{-1} \tag{A1}$$

with

$$N_a(p) = \begin{cases} (250 + 7)\,cm^{-3}, & if\ p \geq 800 hPa \\ (250 \cdot e^{\frac{p-800\,hPa}{150\,hPa}} + 7 \cdot e^{\frac{p-800\,hPa}{400\,hPa}})\,cm^{-3}, & else \end{cases}$$

and

$$B(p) = b_1 \cdot e^{-b_2 \cdot p + b_3}$$
$$C(p) = c_1 \cdot e^{-c_2 \cdot p + c_3}$$
$$b_1 = 3.46281429e + 00, b_2 = 1.74926665e - 04, b_3 = -2.85967514e - 01$$
$$c_1 = 2.72664755e + 00, b_2 = 1.12852352e - 03, c_3 = 1.50069026e + 00.$$

CCN activation was limited to temperatures above -38 °C to prevent production of very large ice number concentrations by CCN activation at low temperatures and immediate subsequent homogeneous freezing of the activated cloud droplets. Vertical
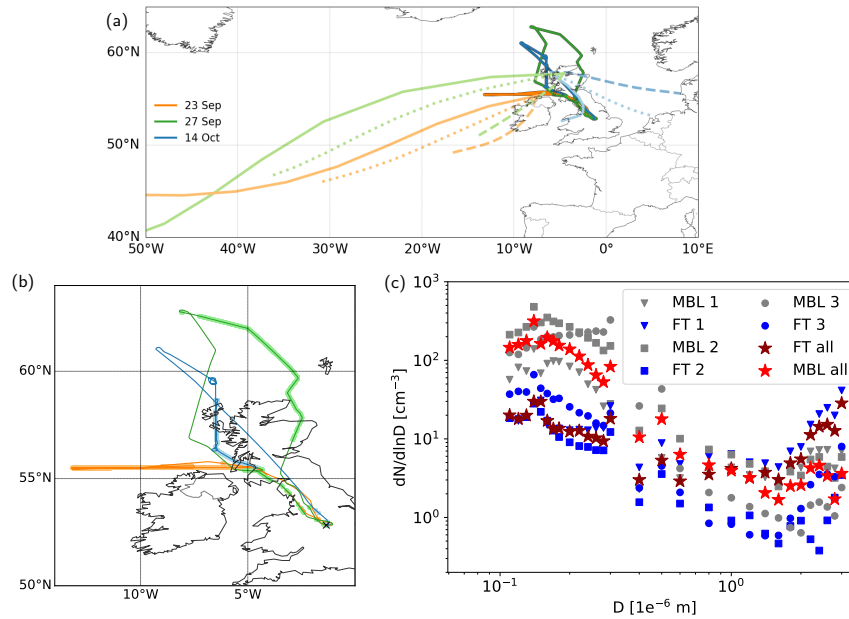
Figure A1. (a) Flight tracks for the NAWDEX British FAAM flights on 23 Sep 2016 (orange), 27 Sep 2016 (green), and 14 Oct 2016 (blue) including mean 24-h backward trajectories from the flight tracks for all three flights (colored in orange, green, and blue, respectively). Trajectory positions are averaged and shown for the lower (dashed lines, $p > 850\,hPa$), middle (dotted lines, $850\,hPa > p > 300\,hPa$) and upper (solid lines, $p < 300\,hPa$) troposphere. **(b)** Zoomed in flight tracks of **(a)**. The highlighted tracks show regions where data are available. **(c)** Median log-normal aerosol size distribution for the marine boundary layer (MBL) and the free troposphere (FT) for measurements from all three flights and from the flights individually.

790 profiles of the predicted CCN number densities from the original parameterisation by Hande et al. (2016) (dashed lines) and our modified version (solid lines) are shown in Fig. 2.

Appendix B: Comparison of modified and original CCN activation scheme

The influence of the modification of the CCN activation scheme has been tested in a limited-area setup for the case study presented in detail above. Figure B1 shows averaged vertical profiles of hydrometeor number concentrations, water content, and selected diabatic heating rates in the WCB cloud band from two 24-h limited-area simulations using the (i) original and (ii) modified Hande scheme (in both simulations CCN activation was limited to temperatures above -38 °C). Both limited-area simulations were run for 24 h on the R03B09 grid and are initialized at 00 UTC 04 Oct 2016 from the ICON analysis. Lateral boundary conditions are provided every 3 h from ICON analysis fields. As expected, the CCN activation with the modified CCN activation scheme is reduced, in particular in the lower troposphere (Fig. B1c). This is associated with an expected reduction in cloud droplet number concentrations and cloud water content, while rain water content and number concentrations are increased (Fig. B1a,b). Although the effect on averaged vertical profiles of diabatic heating rates, such as condensation, evaporation, and vapor deposition on ice hydrometeors is relatively small (Fig. B1d), some difference in averaged diabatic heating rates are discernible that may influence WCB ascent (Fig. B1d).
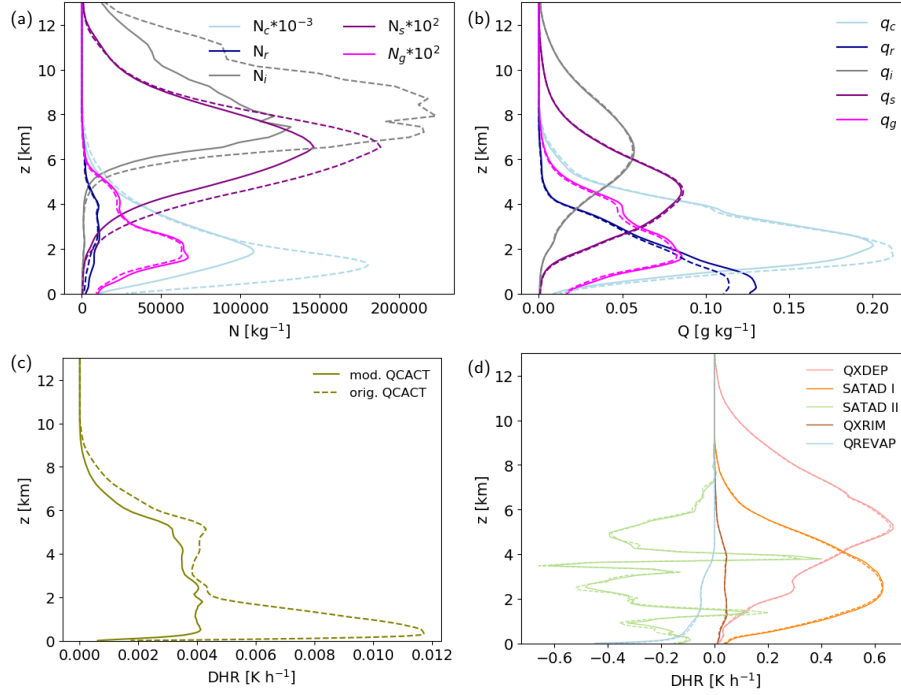
Figure B1. Averaged vertical profiles in the WCB cloud band (selected as region where total water path exceeds $1\,\mathrm{kg\,m^{-2}}$) from two 24-h long limited-area simulations of the WCB case study illustrating the differences that arise from a modification of the original CCN activation scheme. Solid lines show results from a simulation with the modified CCN activation scheme, and dashed lines show results from the original CCN activation scheme. Shown is **(a)** hydrometeor number concentrations (N, in $\mathrm{kg^{-1}}$)), **(b)** hydrometeor masses (q, in $\mathrm{g\,kg^{-1}}$), **(c)** diabatic heating rate from CCN activation (DHR, in $\mathrm{K\,h^{-1}}$), and **(d)** diabatic heating rates (DHR, in $\mathrm{K\,h^{-1}}$) from both saturation adjustments (SATAD I and II), vapor deposition (QXDEP), riming (QXRIM), and evaporation of rain (QREVAP).

Author contributions. AKM and AO implemented the additional online diagnostics and performed the analysis. All authors continuously discussed the results and contributed to the final manuscript.

Competing interests. The authors declare that they have no conflict of interest.

Acknowledgements. The research leading to these results has been done within the subproject B8 of the Transregional Collaborative Research Center SFB / TRR 165 "Waves to Weather" (www.wavestoweather.de) funded by the German Research Foundation (DFG). CMG is supported by the Helmholtz Association as part of the Young Investigator Group "Sub-seasonal Predictability: Understanding the Role of Diabatic Outflow" (SPREADOUT, grant VH-NG-1243). The authors acknowledge support by the state of Baden-Württemberg through bwHPC. The high-resolution ICON simulation was performed on the supercomputer Mogon-II at Johannes Gutenberg University Mainz, which is a member of the AHRP (Alliance for High Performance Computing in Rhineland Palatinate) and the Gauss Alliance e.V. . The development of the special diagnostics in ICON was additionally carried out on the supercomputers ForHLR II and HoreKa at Karlsruhe Institute of Technology Karlsruhe, which are funded by the Ministry of Science, Research and the Arts Baden-Württemberg, Germany, and the German Federal Ministry of Education and Research. The authors gratefully acknowledge the computing time granted on the supercomputers Mogon-II at Johannes Gutenberg University Mainz and on ForHLR II and HoreKa at Karlsruhe Institute of Technology Karlsruhe. The authors kindly acknowledge the CEDA data archive for providing access to the FAAM flight data.

References

Attinger, R., Spreitzer, E., Boettcher, M., Forbes, R., Wernli, H., and Joos, H.: Quantifying the role of individual diabatic processes for the formation of PV anomalies in a North Pacific cyclone, Q. J. R. Meteorol. Soc., 145, https://doi.org/10.1002/qj.3573, 2019.

Attinger, R., Spreitzer, E., Boettcher, M., Wernli, H., and Joos, H.: Systematic assessment of the diabatic processes that modify low-level potential vorticity in extratropical cyclones, Weather Clim. Dynam., 2, 1073–1091, https://doi.org/10.5194/wcd-2-1073-2021, 2021.

Barthlott, C. and Hoose, C.: Aerosol effects on clouds and precipitation over Central Europe in different weather regimes, J. Atmos. Sci., 75, 4247 – 4264, https://doi.org/10.1175/JAS-D-18-0110.1, 2018.

Barthlott, C., Mühr, B., and Hoose, C.: Sensitivity of the 2014 Pentecost storms over Germany to different model grids and microphysics schemes, Q. J. R. Meteorol. Soc., 143, 1485–1503, https://doi.org/https://doi.org/10.1002/qj.3019, 2017.

Barthlott, C., Zarboo, A., Matsunobu, T., and Keil, C.: Importance of aerosols and shape of the cloud droplet size distribution for convective clouds and precipitation, Atmos. Chem. Phys., 22, 2153–2172, https://doi.org/10.5194/acp-22-2153-2022, 2022.

Baumgart, M., Ghinassi, P., Wirth, V., Selz, T., Craig, G. C., and Riemer, M.: Quantitative view on the processes governing the upscale error growth up to the planetary scale using a stochastic convection scheme, Mon. Wea. Rev., 147, 1713–1731, https://doi.org/10.1175/MWR-D-18-0292.1, 2019.

Bechtold, P., Köhler, M., Jung, T., Doblas-Reyes, F., Leutbecher, M., Rodwell, M. J., Vitart, F., and Balsamo, G.: Advances in simulating atmospheric variability with the ECMWF model: From synoptic to decadal time-scales, Q. J. R. Meteorol. Soc., 134, 1337–1351, https://doi.org/10.1002/qj.289, 2008.

Berman, J. D. and Torn, R. D.: The impact of initial condition and warm conveyor belt forecast uncertainty on variability in the downstream waveguide in an ECWMF case study, Mon. Wea. Rev., 147, 4071–4089, https://doi.org/10.1175/MWR-D-18-0333.1, 2019.

Bigg, E. K.: The formation of atmospheric ice crystals by the freezing of droplets, Q. J. R. Meteorol. Soc., 79, 510–519, https://doi.org/https://doi.org/10.1002/qj.49707934207, 1953.

Binder, H., Boettcher, M., Joos, H., and Wernli, H.: The role of warm conveyor belts for the intensification of extratropical cyclones in Northern Hemisphere winter, J. Atmos. Sci., 73, 3997–4020, https://doi.org/10.1175/JAS-D-15-0302.1, 2016.

Blanchard, N., Pantillon, F., Chaboureau, J.-P., and Delanoë, J.: Organization of convective ascents in a warm conveyor belt, Weather Clim. Dynam., 1, 617–634, https://doi.org/10.5194/wcd-1-617-2020, 2020.

Blanchard, N., Pantillon, F., Chaboureau, J.-P., and Delanoë, J.: Mid-level convection in a warm conveyor belt accelerates the jet stream, Weather Clim. Dynam., 2, 37–53, https://doi.org/10.5194/wcd-2-37-2021, 2021.

Boettcher, M. and Wernli, H.: A 10-yr climatology of diabatic Rossby waves in the Northern Hemisphere, Mon. Wea. Rev., 141, 1139–1154, https://doi.org/10.1175/MWR-D-12-00012.1, 2013.

Boettcher, M., Schäfler, A., Sprenger, M., Sodemann, H., Kaufmann, S., Voigt, C., Schlager, H., Summa, D., Di Girolamo, P., Nerini, D., Germann, U., and Wernli, H.: Lagrangian matches between observations from aircraft, lidar and radar in a warm conveyor belt crossing orography, Atmospheric Chemistry and Physics, 21, 5477–5498, https://doi.org/10.5194/acp-21-5477-2021, 2021.

CEDA, Centre for Environmental Data Analysis: https://catalogue.ceda.ac.uk, accessed 04/2021], 2016.

CEDA, Facility for Airborne Atmospheric Measurements; Natural Environment Research Council; Met Office: FAAM B984 ISMAR and T-NAWDEX flight: Airborne atmospheric measurements from core instrument suite on board the BAE-146 aircraft, https://catalogue.ceda.ac.uk/uuid/46ca2a2cc8ce497fbf06beaf31f67098, Centre for Environmental Data Analysis, accessed 04/2021], 2016a.

855 CEDA, Facility for Airborne Atmospheric Measurements; Natural Environment Research Council; Met Office: FAAM B981 T-NAWDEX flight: Airborne atmospheric measurements from core instrument suite on board the BAE-146 aircraft, https://catalogue.ceda.ac.uk/uuid/eef7311cd4374738ad0272e0df189f34, Centre for Environmental Data Analysis, accessed 04/2021], 2016b.

CEDA, Facility for Airborne Atmospheric Measurements; Natural Environment Research Council; Met Office: FAAM B980 T-NAWDEX flight: Airborne atmospheric measurements from core instrument suite on board the BAE-146 aircraft, https://catalogue.ceda.ac.uk/uuid/d802040267e141019fad89bf25b85675, Centre for Environmental Data Analysis, accessed 04/2021], 2016c.

860 Chagnon, J. M. and Gray, S. L.: Horizontal potential vorticity dipoles on the convective storm scale, Q. J. R. Meteorol. Soc., 135, 1392–1408, https://doi.org/10.1002/qj.468, 2009.

Choudhary, A. and Voigt, A.: Impact of grid spacing, convective parameterization and cloud microphysics in ICON simulations of a warm conveyor belt, Weather Clim. Dynam., 3, 1199–1214, https://doi.org/10.5194/wcd-3-1199-2022, 2022.

Crespo, J. A. and Posselt, D. J.: A-Train-based case study of stratiform - convective transition within a warm conveyor belt, Mon. Wea. Rev., 865 144, 2069–2084, https://doi.org/10.1175/MWR-D-15-0435.1, 2016.

Crezee, B., Joos, H., and Wernli, H.: The microphysical building blocks of low-level potential vorticity anomalies in an idealized extratropical cyclone, J. Atmos. Sci., 74, 1403–1416, https://doi.org/10.1175/JAS-D-16-0260.1, 2017.

Dearden, C., Vaughan, G., Tsai, T., and Chen, J.-P.: Exploring the diabatic role of ice microphysical processes in two North Atlantic summer cyclones, Mon. Wea. Rev., 144, 1249 – 1272, https://doi.org/10.1175/MWR-D-15-0253.1, 2016.

870 Droplet Measurement Technologies: Operator Manual: Passive Cavity Aerosol Spectrometer Probe (PCASP-100X), https://www.dropletmeasurement.com/manual/operations-manual-passive-cavity-aerosol-spectrometer-probe-pcasp-100x/, [accessed 01/2022], 2017.

Eckhardt, S., Stohl, A., Wernli, H., James, P., Forster, C., and Spichtinger, N.: A 15-Year climatology of warm conveyor belts, J. Climate, 17, 218–237, https://doi.org/10.1175/1520-0442(2004)017<0218:AYCOWC>2.0.CO;2, 2004.

ECMWF: IFS Documentation CY43R1 - Part IV: Physical processes, ECMWF Rep., https://doi.org/10.21957/sqvo5yxja, 2016.

875 Fan, J., Wang, Y., Rosenfeld, D., and Liu, X.: Review of aerosol–cloud interactions: Mechanisms, significance, and challenges, J. Atmos. Sci., 73, 4221 – 4252, https://doi.org/10.1175/JAS-D-16-0037.1, 2016.

Field, P. R., Lawson, R. P., Brown, P. R. A., Lloyd, G., Westbrook, C., Moisseev, D., Miltenberger, A., Nenes, A., Blyth, A., Choularton, T., Connolly, P., Buehl, J., Crosier, J., Cui, Z., Dearden, C., DeMott, P., Flossmann, A., Heymsfield, A., Huang, Y., Kalesse, H., Kanji, Z. A., Korolev, A., Kirchgaessner, A., Lasher-Trapp, S., Leisner, T., McFarquhar, G., Phillips, V., Stith, J., and Sullivan, S.: 880 Secondary ice production: Current state of the science and recommendations for the future, Meteorol. Monographs, 58, 7.1 – 7.20, https://doi.org/10.1175/AMSMONOGRAPHS-D-16-0014.1, 2017.

Flack, D. L. A., Rivière, G., Musat, I., Roehrig, R., Bony, S., Delanoë, J., Cazenave, Q., and Pelon, J.: Representation by two climate models of the dynamical and diabatic processes involved in the development of an explosively deepening cyclone during NAWDEX, Weather Clim. Dynam., 2, 233–253, https://doi.org/10.5194/wcd-2-233-2021, 2021.

885 Forbes, R. M. and Clark, P. A.: Sensitivity of extratropical cyclone mesoscale structure to the parametrization of ice microphysical processes, Q. J. R. Meteorol. Soc., 129, 1123–1148, https://doi.org/https://doi.org/10.1256/qj.01.171, 2003.

Gehring, J., Oertel, A., Vignon, E., Jullien, N., Besic, N., and Berne, A.: Microphysics and dynamics of snowfall associated with a warm conveyor belt over Korea, Atmos. Chem. Phys., 20, 7373–7392, https://doi.org/10.5194/acp-20-7373-2020, 2020.

Grams, C., Beerli, R., Pfenninger, S., Staffell, I., and Wernli, H.: Balancing Europe's wind power output through spatial deployment informed 890 by weather regimes., Nat. Clim. Chang., 7, 557–562, https://doi.org/10.1038/nclimate3338, 2017.

Grams, C. M. and Archambault, H. M.: The key role of diabatic outflow in amplifying the midlatitude flow: a representative case study of weather systems surrounding western North Pacific extratropical transition, Mon. Wea. Rev., 144, https://doi.org/10.1175/MWR-D-15-0419.1, 2016.

Grams, C. M., Wernli, H., Boettcher, M., Čampa, J., Corsmeier, U., Jones, S. C., Keller, J. H., Lenz, C.-J., and Wiegand, L.: The key role of diabatic processes in modifying the upper-tropospheric wave guide: a North Atlantic case-study, Q. J. R. Meteor. Soc., 137, 2174–2193, https://doi.org/10.1002/qj.891, 2011.

Grams, C. M., Magnusson, L., and Madonna, E.: An atmospheric dynamics perspective on the amplification and propagation of forecast error in numerical weather prediction models: A case study, Q. J. R. Meteor. Soc., 144, 2577–2591, https://doi.org/10.1002/qj.3353, 2018.

Hande, L. B. and Hoose, C.: Partitioning the primary ice formation modes in large eddy simulations of mixed-phase clouds, Atmos. Chem. and Phys., 17, 14 105–14 118, https://doi.org/10.5194/acp-17-14105-2017, 2017.

Hande, L. B., Engler, C., Hoose, C., and Tegen, I.: Seasonal variability of Saharan desert dust and ice nucleating particles over Europe, Atmos. Chem. Phys., 15, 4389–4397, https://doi.org/10.5194/acp-15-4389-2015, 2015.

Hande, L. B., Engler, C., Hoose, C., and Tegen, I.: Parameterizing cloud condensation nuclei concentrations during HOPE, Atmos. Chem. Phys., 16, 12 059–12 079, https://doi.org/10.5194/acp-16-12059-2016, 2016.

Harvey, B., Methven, J., Sanchez, C., and Schäfler, A.: Diabatic generation of negative potential vorticity and its impact on the North Atlantic jet stream, Q. J. R. Meteorol. Soc., 146, 1477–1497, https://doi.org/10.1002/qj.3747, 2020.

Hersbach, H., Bell, W., Berrisford, P., Horányi, A., Sabater, J. M., Nicolas, J., Radu, R., Schepers, D., Simmons, A., Soci, C, D., and D: Global reanalysis: goodbye ERA-Interim, hello ERA5, ECMWF Newsletter, 159, 17–24, https://doi.org/10.21957/vf291hehd7, 2019.

Hersbach, H., Bell, B., Berrisford, P., Hirahara, S., Horányi, A., Muñoz-Sabater, J., Nicolas, J., Peubey, C., Radu, R., Schepers, D., Simmons, A., Soci, C., Abdalla, S., Abellan, X., Balsamo, G., Bechtold, P., Biavati, G., Bidlot, J., Bonavita, M., De Chiara, G., Dahlgren, P., Dee, D., Diamantakis, M., Dragani, R., Flemming, J., Forbes, R., Fuentes, M., Geer, A., Haimberger, L., Healy, S., Hogan, R. J., Hólm, E., Janisková, M., Keeley, S., Laloyaux, P., Lopez, P., Lupu, C., Radnoti, G., de Rosnay, P., Rozum, I., Vamborg, F., Villaume, S., and Thépaut, J.-N.: The ERA5 global reanalysis, Q. J. R. Meteorol. Soc., 146, 1999–2049, https://doi.org/https://doi.org/10.1002/qj.3803, 2020.

Hudson, J. G. and Xie, Y.: Vertical distributions of cloud condensation nuclei spectra over the summertime northeast Pacific and Atlantic Oceans, J. Geophys. Res.: Atmospheres, 104, 30 219–30 229, https://doi.org/https://doi.org/10.1029/1999JD900413, 1999.

Igel, A. L. and van den Heever, S. C.: Invigoration or enervation of convective clouds by aerosols?, Geophys. Res. Lett., 48, e2021GL093 804, https://doi.org/https://doi.org/10.1029/2021GL093804, 2021.

Jeffery, C. A. and Austin, P. H.: Homogeneous nucleation of supercooled water: Results from a new equation of state, J. Geophys. Res.: Atmospheres, 102, 25 269–25 279, https://doi.org/https://doi.org/10.1029/97JD02243, 1997.

Joos, H.: Warm conveyor belts and their role for cloud radiative forcing in the extratropical storm tracks, J. Climate, 32, 5325–5343, https://doi.org/10.1175/JCLI-D-18-0802.1, 2019.

Joos, H. and Forbes, R. M.: Impact of different IFS microphysics on a warm conveyor belt and the downstream flow evolution, Q. J. R. Meteorol. Soc., 142, 2727–2739, https://doi.org/10.1002/qj.2863, 2016.

Joos, H. and Wernli, H.: Influence of microphysical processes on the potential vorticity development in a warm conveyor belt: a case-study with the limited-area model COSMO, Q. J. R. Meteorol. Soc., 138, 407–418, https://doi.org/10.1002/qj.934, 2012.

Joos, H., Spichtinger, P., Reutter, P., and Fusina, F.: Influence of heterogeneous freezing on the microphysical and radiative properties of orographic cirrus clouds, Atmos. Chem. Phys., 14, 6835–6852, https://doi.org/10.5194/acp-14-6835-2014, 2014.

Joos, H., Madonna, E., Witlox, K., Ferrachat, S., Wernli, H., and Lohmann, U.: Effect of anthropogenic aerosol emissions on precipitation in warm conveyor belts in the western North Pacific in winter – a model study with ECHAM6-HAM, Atmospheric Chemistry and Physics, 17, 6243–6255, https://doi.org/10.5194/acp-17-6243-2017, 2017.

Joos, H., Sprenger, M., Binder, H., Beyerle, U., and Wernli, H.: Warm conveyor belts in present-day and future climate simulations – Part 1: Climatology and impacts, Wea. Clim. Dynam., 4, 133–155, https://doi.org/10.5194/wcd-4-133-2023, 2023.

Kärcher, B. and Lohmann, U.: A parameterization of cirrus cloud formation: Homogeneous freezing of supercooled aerosols, J. Geophys. Res.: Atmospheres, 107, AAC 4–1–AAC 4–10, https://doi.org/https://doi.org/10.1029/2001JD000470, 2002.

Kärcher, B., Hendricks, J., and Lohmann, U.: Physically based parameterization of cirrus cloud formation for use in global atmospheric models, J. Geophys. Res.: Atmospheres, 111, D01 205, https://doi.org/https://doi.org/10.1029/2005JD006219, 2006.

Khain, A. P., Beheng, K. D., Heymsfield, A., Korolev, A., Krichak, S. O., Levin, Z., Pinsky, M., Phillips, V., Prabhakaran, T., Teller, A., van den Heever, S. C., and Yano, J.-I.: Representation of microphysical processes in cloud-resolving models: Spectral (bin) microphysics versus bulk parameterization, Rev. Geophys., 53, 247–322, https://doi.org/https://doi.org/10.1002/2014RG000468, 2015.

Krämer, M., Rolf, C., Luebke, A., Afchine, A., Spelten, N., Costa, A., Meyer, J., Zöger, M., Smith, J., Herman, R. L., Buchholz, B., Ebert, V., Baumgardner, D., Borrmann, S., Klingebiel, M., and Avallone, L.: A microphysics guide to cirrus clouds – Part 1: Cirrus types, Atmos. Chem. Phys., 16, 3463–3483, https://doi.org/10.5194/acp-16-3463-2016, 2016.

Leuenberger, D., Koller, M., Fuhrer, O., and Schär, C.: A generalization of the SLEVE vertical coordinate, Mon. Wea. Rev., 141, 3683–3689, https://doi.org/10.1175/2010MWR3307.1, 2010.

Lott, F. and Miller, M. J.: A new subgrid-scale orographic drag parametrization: Its formulation and testing., Q. J. R. Meteorol. Soc, 123, 101–127, https://doi.org/10.1002/qj.49712353704, 1997.

Luebke, A. E., Afchine, A., Costa, A., Grooß, J.-U., Meyer, J., Rolf, C., Spelten, N., Avallone, L. M., Baumgardner, D., and Krämer, M.: The origin of midlatitude ice clouds and the resulting influence on their microphysical properties, Atmos. Chem. Phys., 16, 5793–5809, https://doi.org/10.5194/acp-16-5793-2016, 2016.

Maddison, J. W., Gray, S. L., Martínez-Alvarado, O., and Williams, K. D.: Upstream cyclone influence on the predictability of block onsets over the Euro-Atlantic Region, Mon. Wea. Rev., 147, 1277–1296, https://doi.org/10.1175/MWR-D-18-0226.1, 2019.

Madonna, E., Wernli, H., Joos, H., and Martius, O.: Warm conveyor belts in the ERA-Interim dataset (1979-2010). Part I: Climatology and potential vorticity evolution, J. Climate, 27, 3–26, https://doi.org/10.1175/JCLI-D-12-00720.1, 2014.

Marinescu, P. J., van den Heever, S. C., Heikenfeld, M., Barrett, A. I., Barthlott, C., Hoose, C., Fan, J., Fridlind, A. M., Matsui, T., Miltenberger, A. K., Stier, P., Vié, B., White, B. A., and Zhang, Y.: Impacts of varying concentrations of cloud condensation nuclei on deep convective cloud updrafts - A multimodel assessment, J. Atmos. Sci., 78, 1147 – 1172, https://doi.org/10.1175/JAS-D-20-0200.1, 2021.

Martínez-Alvarado, O., Joos, H., Chagnon, J., Boettcher, M., Gray, S. L., Plant, R. S., Methven, J., and Wernli, H.: The dichotomous structure of the warm conveyor belt, Q. J. R. Meteorol. Soc., 140, 1809–1824, https://doi.org/10.1002/qj.2276, 2014.

Mazoyer, M., Ricard, D., Rivière, G., Delanoë, J., Arbogast, P., Vié, B., Lac, C., Cazenave, Q., and Pelon, P.: Microphysics impacts on the warm conveyor belt and ridge building of the NAWDEX IOP6 cyclone, Mon. Wea. Rev., 149, 3961–3980, https://doi.org/10.1175/MWR-D-21-0061.1, 2021.

Mazoyer, M., Ricard, D., Rivière, G., Delanoö, J., Riette, S., Augros, C., Borderies, M., and Vié, B.: Impact of mixed-phase cloud parameterization on warm conveyor belts and upper-tropospheric dynamics, Mon. Wea. Rev., 151, 1073–1091, https://doi.org/10.1175/MWR-D-22-0045.1, 2023.

McCoy, D. T., Field, P. R., Schmidt, A., Grosvenor, D. P., Bender, F. A.-M., Shipway, B. J., Hill, A. A., Wilkinson, J. M., and Elsaesser, G. S.: Aerosol midlatitude cyclone indirect effects in observations and high-resolution simulations, Atmos. Chem. Phys., 18, 5821–5846, https://doi.org/10.5194/acp-18-5821-2018, 2018.

Methven, J.: Potential vorticity in warm conveyor belt outflow, Q. J. R. Meteor. Soc., 141, 1065–1071, https://doi.org/10.1002/qj.2393, 2015.

Miltenberger, A. K., Pfahl, S., and Wernli, H.: An online trajectory module (version 1.0) for the nonhydrostatic numerical weather prediction model COSMO, Geosci. Model Dev., 6, 1989–2004, https://doi.org/10.5194/gmd-6-1989-2013, 2013.

Miltenberger, A. K., Roches, A., Pfahl, S., and Wernli, H.: Online trajectory module in COSMO: A short user guide, COSMO Technical Report 24, 2014.

Miltenberger, A. K., Reynolds, S., and Sprenger, M.: Revisiting the latent heating contribution to foehn warming: Lagrangian analysis of two foehn events over the Swiss Alps, Q. J. R. Meteorol. Soc., 142, 2194–2204, https://doi.org/https://doi.org/10.1002/qj.2816, 2016.

Miltenberger, A. K., Lüttmer, T., and Siewert, C.: Secondary ice formation in idealised deep convection - Source of primary ice and impact on glaciation, Atmosphere, 11, https://doi.org/10.3390/atmos11050542, 2020.

Mlawer, E. J., Taubman, S. J., Brown, P. D., Iacono, M. J., and Clough, S. A.: Radiative transfer for inhomogeneous atmospheres: RRTM, a validated correlated-k model for the longwave, J. Geophys. Res.: Atmos., 102, 16 663–16 682, https://doi.org/10.1029/97JD00237, 1997.

Morrison, H., Curry, J. A., and Khvorostyanov, V. I.: A new double-moment microphysics parameterization for application in cloud and climate models. Part I: Description, J. Atmos. Sci., 62, 1665–1677, https://doi.org/10.1175/JAS3446.1, 2005.

Noppel, H., Blahak, U., Seifert, A., and Beheng, K. D.: Simulations of a hailstorm and the impact of CCN using an advanced two-moment cloud microphysical scheme, Atmos. Res., 96, 286–301, https://doi.org/https://doi.org/10.1016/j.atmosres.2009.09.008, 2010.

Nott, G.: FAAM CORE Passive Cavity Aerosol Spectrometer Probe, https://old.faam.ac.uk/index.php/science-instruments/aerosol/304-pcasp, [accessed 01/2022], 2013.

Oertel, A. and Schemm, S.: Quantifying the circulation induced by convective clouds in kilometer-scale simulations, Q. J. R. Meteorol. Soc., 2021.

Oertel, A., Boettcher, M., Joos, H., Sprenger, M., Konow, H., Hagen, M., and Wernli, H.: Convective activity in an extratropical cyclone and its warm conveyor belt - a case-study combining observations and a convection-permitting model simulation, Q. J. R. Meteorol. Soc., 145, 1406–1426, https://doi.org/10.1002/qj.3500, 2019.

Oertel, A., Boettcher, M., Joos, H., Sprenger, M., and Wernli, H.: Potential vorticity structure of embedded convection in a warm conveyor belt and its relevance for large-scale dynamics, Weather Clim. Dynam., 1, 127–153, https://doi.org/10.5194/wcd-1-127-2020, 2020.

Oertel, A., Sprenger, M., Joos, H., Boettcher, M., Konow, H., Hagen, M., and Wernli, H.: Observations and simulation of intense convection embedded in a warm conveyor belt – how ambient vertical wind shear determines the dynamical impact, Weather Clim. Dynam., 2, 89–110, https://doi.org/10.5194/wcd-2-89-2021, 2021.

Oertel, A., Pickl, M., Quinting, J. F., Hauser, S., Wandel, J., Magnusson, L., Balmaseda, M., Vitart, F., and Grams, C. M.: Everything hits at once: How remote rainfall matters for the prediction of the 2021 North American heat wave, Geophys. Res. Lett., 50, e2022GL100 958, https://doi.org/https://doi.org/10.1029/2022GL100958, 2023.

Ollinaho, P., Lock, S.-J., Leutbecher, M., Bechtold, P., Beljaars, A., Bozzo, A., Forbes, R. M., Haiden, T., Hogan, R. J., and Sandu, I.: Towards process-level representation of model uncertainties: stochastically perturbed parametrizations in the ECMWF ensemble, Q. J. R. Meteorol. Soc., 143, 408–422, https://doi.org/https://doi.org/10.1002/qj.2931, 2017.

Orr, A., Bechtold, P., Scinocca, J., Ern, M., and Janiskova, M.: Improved middle atmosphere climate and forecasts in the ECMWF model through a nonorographic gravity wave drag parameterization., J. Clim., 23, 5905–5926, https://doi.org/10.1175/2010JCLI3490, 2010.

Papritz, L., Aemisegger, F., and Wernli, H.: Sources and transport pathways of precipitating waters in cold-season deep North Atlantic cyclones, J. Atmos. Sci., 78, 3349 – 3368, https://doi.org/10.1175/JAS-D-21-0105.1, 2021.

1005 Pfahl, S., Madonna, E., Boettcher, M., Joos, H., and Wernli, H.: Warm conveyor belts in the ERA-Interim data set (1979-2010). Part II: Moisture origin and relevance for precipitation, J. Climate, 27, 27–40, https://doi.org/10.1175/JCLI-D-13-00223.1, 2014.

Pickl, M., Lang, S. T. K., Leutbecher, M., and Grams, C. M.: The effect of stochastically perturbed parametrisation tendencies (SPPT) on rapidly ascending air streams, Q. J. R. Meteorol. Soc., 148, 1242–1261, https://doi.org/https://doi.org/10.1002/qj.4257, 2022.

Pomroy, H. R. and Thorpe, A. J.: The evolution and dynamical role of reduced upper-tropospheric potential vorticity in intensive observ-
1010 ing period one of FASTEX, Mon. Wea. Rev., 128, 1817–1834, https://doi.org/10.1175/1520-0493(2000)128<1817:TEADRO>2.0.CO;2, 2000.

Quinting, J. F. and Grams, C. M.: EuLerian Identification of ascending AirStreams (ELIAS 2.0) in numerical weather prediction and climate models - Part 1: Development of deep learning model, Geosci. Model Dev., 15, 715–730, https://doi.org/10.5194/gmd-15-715-2022, 2022.

Quinting, J. F., Grams, C. M., Oertel, A., and Pickl, M.: EuLerian Identification of ascending AirStreams (ELIAS 2.0) in numer-
1015 ical weather prediction and climate models - Part 2: Model application to different datasets, Geosci. Model Dev., 15, 731–744, https://doi.org/10.5194/gmd-15-731-2022, 2022.

Raschendorfer, M.: The new turbulence parameterization of LM, Cosmo news letter no. 1, Consortium for Small-Scale Modelling, [avail-able from http://www.cosmo-model.org/content/model/documentation/newsLetters/newsLetter01/newsLetter_01.pdf, accessed 12/2021], 2018.

1020 Rasp, S., Selz, T., and Craig, G.: Convective and slantwise trajectory ascent in convection-permitting simulations of midlatitude cyclones, Mon. Wea. Rev., 144, 3961–3976, https://doi.org/10.1175/MWR-D-16-0112.1, 2016.

Reed, R. J., Stoelinga, M. T., and Kuo, Y.-H.: A model-aided study of the origin and evolution of the anomalously high potential vorticity in the inner region of a rapidly deepening marine cyclone, Mon. Wea. Rev., 120, 893–913, https://doi.org/10.1175/1520-0493(1992)120<0893:AMASOT>2.0.CO;2, 1992.

1025 Rivière, G., Wimmer, M., Arbogast, P., Piriou, J.-M., Delanoë, J., Labadie, C., Cazenave, Q., and Pelon, J.: The impact of deep convection representation in a global atmospheric model on the warm conveyor belt and jet stream during NAWDEX IOP6, Weather Clim. Dynam., 2, 1011–1031, https://doi.org/10.5194/wcd-2-1011-2021, 2021.

Rodwell, M., Forbes, R., and Wernli, H.: Why warm conveyor belts matter in NWP, ECMWF Newsletter, 154, 21–28, https://doi.org/10.21957/mr20vg, 2017.

1030 Rossa, A., Wernli, H., and Davies, H. C.: Growth and decay of an extra-tropical cyclone's PV-tower, Meteorol. Atmos. Phys., 73, 139–156, https://doi.org/10.1007/s007030050070, 2000.

Rothenberg, D. and Wang, C.: Metamodeling of droplet activation for global climate models, J. Atmos. Sci., 73, 1255–1272, https://doi.org/10.1175/JAS-D-15-0223.1, 2016.

Saffin, L., Methven, J., Bland, J., Harvey, B., and Sanchez, C.: Circulation conservation in the outflow of warm conveyor belts and conse-
1035 quences for Rossby wave evolution, Q. J. R. Meteorol. Soc., 147, 3587–3610, https://doi.org/https://doi.org/10.1002/qj.4143, 2021.

Schäfler, A. and Harnisch, F.: Impact of the inflow moisture on the evolution of a warm conveyor belt, Q. J. R. Meteorol. Soc., 141, 299–310, https://doi.org/10.1002/qj.2360, 2015.

Schäfler, A., Craig, C., Wernli, H., Arbogast, P., Doyle, J. D., McTaggart-Cowan, R., Methven, J., Rivière, G., Ament, F., Boettcher, M., Bramberger, M., Cazenave, Q., Cotton, R., Crewell, S., Delanoë, J., Dörnbrack, A., Ehrlich, A., Ewald, F., Fix, A., Grams, C. M., Gray,
1040 S. L., Grob, H., Groß, S., Hagen, M., Harvey, B., Hirsch, L., Jacob, M., Kölling, T., Konow, H., Lemmerz, C., Lux, O., Magnusson, L.,

Mayer, B., Mech, M., Moore, R., Pelon, J., Quinting, J., Rahm, S., Rapp, M., Rautenhaus, M., Reitebuch, O., Reynolds, C. A., Sodemann, H., Spengler, T., Vaughan, G., Wendisch, M., Wirth, M., Witschas, B., Wolf, K., and Zinner, T.: The North Atlantic Waveguide and Downstream Impact Experiment, Bull. Am. Meteor. Soc., 99, 1607–1637, https://doi.org/10.1175/BAMS-D-17-0003.1, 2018.

Seifert, A.: On the parameterization of evaporation of raindrops as simulated by a one-dimensional rainshaft model, J. Atmos. Sci., 65, 3608 – 3619, https://doi.org/10.1175/2008JAS2586.1, 2008.

Seifert, A. and Beheng, K.: A two-moment cloud microphysics parameterization for mixed-phase clouds. Part 1: Model description, Meteorol. Atmos. Phys., 92, 45–66, https://doi.org/10.1007/s00703-005-0112-4, 2006a.

Seifert, A. and Beheng, K.: A two-moment cloud microphysics parameterization for mixed-phase clouds. Part 2: Maritime vs. continental deep convective storms, Meteorol. Atmos. Phys., 92, 67–82, https://doi.org/https://doi.org/10.1007/s00703-005-0113-3, 2006b.

Spreitzer, E., Attinger, R., Boettcher, M., Forbes, R., Wernli, H., and Joos, H.: Modification of potential vorticity near the tropopause by nonconservative processes in the ECMWF model, J. Atmos. Sci., 76, 1709–1726, https://doi.org/10.1175/JAS-D-18-0295.1, 2019.

Sprenger, M. and Wernli, H.: The LAGRANTO Lagrangian analysis tool – version 2.0, Geosci. Model Dev., 8, 2569–2586, https://doi.org/10.5194/gmd-8-2569-2015, 2015.

Steinfeld, D. and Pfahl, S.: The role of latent heating in atmospheric blocking dynamics: a global climatology, Clim. Dyn., 53, 6159–6180, https://doi.org/10.1007/s00382-019-04919-6, 2019.

Steinfeld, D., Boettcher, M., Forbes, R., and Pfahl, S.: The sensitivity of atmospheric blocking to upstream latent heating – numerical experiments, Weather and Climate Dynamics, 1, 405–426, https://doi.org/10.5194/wcd-1-405-2020, 2020.

Stoelinga, M. T.: A potential vorticity-based study of the role of diabatic heating and friction in a numerically simulated baroclinic cyclone, Mon. Wea. Rev., 124, 849–874, https://doi.org/10.1175/1520-0493(1996)124<0849:APVBSO>2.0.CO;2, 1996.

Storelvmo, T. and Tan, I.: The Wegener-Bergeron-Findeisen process - Its discovery and vital importance for weather and climate, Meteorolog. Z., 24, 455–461, https://doi.org/10.1127/metz/2015/0626, 2015.

Tao, W.-K., Chen, J.-P., Li, Z., Wang, C., and Zhang, C.: Impact of aerosols on convective clouds and precipitation, Rev. Geophys., 50, https://doi.org/https://doi.org/10.1029/2011RG000369, 2012.

Teubler, F. and Riemer, M.: Potential-vorticity dynamics of troughs and ridges within Rossby wave packets during a 40-year reanalysis period, Weather Clim. Dynam., 2, 535–559, https://doi.org/10.5194/wcd-2-535-2021, 2021.

Tiedtke, M.: A comprehensive mass flux scheme for cumulus parameterization in large-scale models, Mon. Wea. Rev., 117, 1779–1800, https://doi.org/10.1175/1520-0493(1989)117,1779:ACMFSF.2.0.CO;2, 1989.

van den Heever, S. C., Stephens, G. L., and Wood, N. B.: Aerosol indirect effects on tropical convection characteristics under conditions of radiative–convective equilibrium, J. Atmos. Sci., 68, 699 – 718, https://doi.org/10.1175/2010JAS3603.1, 2011.

Wang, Y., Zheng, G., Jensen, M. P., Knopf, D. A., Laskin, A., Matthews, A. A., Mechem, D., Mei, F., Moffet, R., Sedlacek, A. J., Shilling, J. E., Springston, S., Sullivan, A., Tomlinson, J., Veghte, D., Weber, R., Wood, R., Zawadowicz, M. A., and Wang, J.: Vertical profiles of trace gas and aerosol properties over the eastern North Atlantic: variations with season and synoptic condition, Atmos. Chem. Phys., 21, 11 079–11 098, https://doi.org/10.5194/acp-21-11079-2021, 2021.

Wernli, H. and Davies, H. C.: A Lagrangian-based analysis of extratropical cyclones. I: The method and some applications, Q. J. R. Meteor. Soc., 123, 467–489, https://doi.org/10.1256/smsqj.53810, 1997.

Wernli, H., Dirren, S., Liniger, M. A., and Zillig, M.: Dynamical aspects of the life cycle of the winter storm 'Lothar' (24 – 26 December 1999), Q. J. R. Meteor. Soc., 128, 405–429, https://doi.org/10.1256/003590002321042036, 2002.

Wernli, H., Boettcher, M., Joos, H., Miltenberger, A. K., and Spichtinger, P.: A trajectory-based classification of ERA-Interim ice clouds in the region of the North Atlantic storm track, Geophys. Res. Lett., 43, 6657–6664, https://doi.org/10.1002/2016GL068922, 2016.

1080   Wimmer, M., Rivière, G., Arbogast, P., Piriou, J.-M., Delanoë, J., Labadie, C., Cazenave, Q., and Pelon, J.: Diabatic processes modulating the vertical structure of the jet stream above the cold front of an extratropical cyclone: sensitivity to deep convection schemes, Wea. Clim. Dynam., 3, 863–882, https://doi.org/10.5194/wcd-3-863-2022, 2022.

Zängl, G., Reinert, D., Rípodas, P., and Baldauf, M.: The ICON (ICOsahedral Non-hydrostatic) modelling framework of DWD and MPI-M: Description of the non-hydrostatic dynamical core, Q. J. R. Meteorol. Soc., 141, 563–579, https://doi.org/10.1002/qj.2378, 2015.

1085   Zhang, Y., Macke, A., and Albers, F.: Effect of crystal size spectrum and crystal shape on stratiform cirrus radiative forcing, Atmos. Res., 52, 59–75, https://doi.org/10.1016/S0169-8095(99)00026-5, 1999.